AGU PUBLICATIONS

JGR

Journal of Geophysical Research: Earth Surface

RESEARCH ARTICLE

10.1002/2014JF003297

Key Points:

- We develop a linear inverse model to invert river profiles for uplift histories
- We invert 957 African and Australian rivers for Cenozoic uplift rate histories
- Drainage networks have coherent signals recording regional growth of elevation

Correspondence to:
G. G. Roberts and N. J. White,
gareth.roberts@imperial.ac.uk;
njw10@cam.ac.uk

Citation:
Rudge, J. F., G. G. Roberts, N. J. White, and C. N. Richardson (2015), Uplift histories of Africa and Australia from linear inverse modeling of drainage inventories, *J. Geophys. Res. Earth Surf.*, *120*, 894–914, doi:10.1002/2014JF003297.

Received 25 JUL 2014
Accepted 19 FEB 2015
Accepted article online 23 FEB 2015
Published online 29 MAY 2015

Uplift histories of Africa and Australia from linear inverse modeling of drainage inventories

John F. Rudge[1], Gareth G. Roberts[2], Nicky J. White[1], and Christopher N. Richardson[3]

[1]Bullard Laboratories, Department of Earth Sciences, University of Cambridge, Cambridge, UK, [2]Department of Earth Science and Engineering, Imperial College London, London, UK, [3]BP Institute, Bullard Laboratories, University of Cambridge, Cambridge, UK

Abstract We describe and apply a linear inverse model which calculates spatial and temporal patterns of uplift rate by minimizing the misfit between inventories of observed and predicted longitudinal river profiles. Our approach builds upon a more general, nonlinear, optimization model, which suggests that shapes of river profiles are dominantly controlled by upstream advection of kinematic waves of incision produced by spatial and temporal changes in regional uplift rate. Here we use the method of characteristics to solve a version of this problem. A damped, nonnegative, least squares approach is developed that permits river profiles to be inverted as a function of uplift rate. An important benefit of a linearized treatment is low computational cost. We have tested our algorithm by inverting 957 river profiles from both Africa and Australia. For each continent, the drainage network was constructed from a digital elevation model. The fidelity of river profiles extracted from this network was carefully checked using satellite imagery. River profiles were inverted many times to systematically investigate the trade-off between model misfit and smoothness. Spatial and temporal patterns of both uplift rate and cumulative uplift were calibrated using independent geologic and geophysical observations. Uplift patterns suggest that the topography of Africa and Australia grew in Cenozoic times. Inverse modeling of large inventories of river profiles demonstrates that drainage networks contain coherent signals that record the regional growth of elevation.

1. Introduction

Uplift and denudation of the Earth's surface are responses to different tectonic and subplate processes. Conversely, spatial and temporal patterns of uplift rates indirectly contain useful information about these processes. In the continents, considerable effort has been expended to constrain these rates by exploiting a range of techniques. For example, databases of uplift, rock cooling and river incision rates have been built using radiometric dating of emergent marine terraces, (U-Th)/He thermochronometry, clumped-isotope altimetry, optically stimulated luminescence, and the history of sedimentary flux [see, e.g., *Tanaka et al.*, 1997; *Ghosh et al.*, 2006; *Flowers et al.*, 2008; *Galloway et al.*, 2011; *Pedoja et al.*, 2011]. From a global perspective, these databases comprise spot measurements which means that spatial coverage can be limited. In most continents, drainage networks set the pace of denudation [e.g., *Anderson and Anderson*, 2010]. Since these networks are widespread, the notion of combining a quantitative understanding of drainage development with independent calibration is an attractive one. It may be possible to determine spatial and temporal patterns of regional uplift rate, which in turn could improve our understanding of tectonic and subplate processes.

Here we show how linear inverse modeling of longitudinal river profiles, with appropriate calibration, may help to determine uplift rate histories. *Pritchard et al.* [2009] and *Roberts and White* [2010] first showed that individual river profiles can be inverted by varying uplift rate as a function of time. Subsequently, *Roberts et al.* [2012] developed a nonlinear optimization model which fits inventories of river profiles as a function of the spatial and temporal pattern of uplift rate. Their general methodology has several important advantages. For example, the relative significance of advective and diffusive erosional processes can be explored, precipitation rate can be varied through time and space, and *Monte Carlo* inverse modeling can be used to investigate how variations and uncertainties in erosional parameters affect patterns of calculated uplift rate.

A justifiably simpler modeling strategy is amenable to linearization, which greatly speeds up the optimization process [*Pritchard et al.*, 2009; *Goren et al.*, 2014; *Fox et al.*, 2014]. This strategy has two significant benefits. First, the erosional parameter space can be more thoroughly and consistently explored. Second, it becomes more practicable to interrogate large drainage inventories on a continent-wide basis. We develop a damped, nonnegative, least squares algorithm and apply it to drainage inventories from Africa and Australia. This algorithm is motivated by the results of our earlier analysis which exploited nonlinear optimization techniques [e.g., *Paul et al.*, 2014; *Czarnota et al.*, 2014]. It permits assessment of the applicability of the stream power erosional model at a range of spatial and temporal scales. *Goren et al.* [2014] and *Fox et al.* [2014] have also developed a linear inverse model, which differs in terms of both implementation and application.

2. Modeling Strategy

It is generally agreed that the shape of a longitudinal river profile (i.e., elevation, z, as a function of upstream distance, x) is determined by some combination of uplift rate, U, and erosion rate, E, both of which can vary as a function of time and space. Thus,

$$-\frac{\partial z}{\partial t} = E(x,t) + U(x,t), \tag{1}$$

where x is distance from the river mouth and t is time before present day. *Roberts and White* [2010] showed that if the shape of a river profile is known, it is feasible to invert for uplift rate as a function of time and/or space. The crux of this problem lies in knowing the erosional history of a river. Erosion of a river channel is a complex process, which is usually approximated by assuming that two forms of erosion occur. The first form assumes that elevation along a river profile is controlled by headward propagation of steep slopes (i.e., detachment-limited erosion) [*Howard and Kerby*, 1983; *Whipple and Tucker*, 1999]. The second form assumes that elevation is strongly influenced by sedimentary transport (i.e., transport-limited erosion) [*Sklar and Dietrich*, 1998, 2001; *Rosenbloom and Anderson*, 1994; *Whipple and Tucker*, 2002; *Tomkin et al.*, 2003].

Erosion rate can be written as

$$E(x,t) = -v_\circ [PA(x)]^m \left(\frac{\partial z}{\partial x}\right)^n + \kappa(x)\frac{\partial^2 z}{\partial x^2}, \tag{2}$$

where $v_\circ$ is a calibration constant with the dimensions of velocity if $m=0$, P is precipitation rate which can vary with space and time, A is upstream drainage area that can be measured at the present day, m and n are dimensionless erosional constants whose values are much debated, and κ is "erosional diffusivity," which could vary along a river profile (Table 3).

In a series of contributions, *Pritchard et al.* [2009], *Roberts and White* [2010], *Roberts et al.* [2012], and *Paul et al.* [2014] showed that the general inverse model can be posed and solved. They demonstrated that values of the four erosional parameters, $v_\circ$, m, n, and κ, affect residual misfits between observed and predicted river profiles in different ways. There is considerable debate about the values of $v_\circ$, m, and in particular n [e.g., *van der Beek and Bishop*, 2003; *Roberts et al.*, 2012; *Royden and Perron*, 2013; *Mudd et al.*, 2014; *Lague*, 2014]. In general, $v_\circ$ determines the timescale for knickpoint retreat and its value must be independently estimated from geologic constraints (e.g., present-day measurements of incision). Both *Roberts and White* [2010] and *Croissant and Braun* [2014] showed that $v_\circ$ and m trade off negatively with each other so that different combinations of $v_\circ$ and m yield equally acceptable fits between observed and predicted river profiles.

The value of n is subject to much discussion [see, e.g., *Lague*, 2014]. Solutions of the detachment-limited model (i.e., first term on right-hand side of equation (2)) can develop shocks if $n>1$ so that steeper slopes propagate faster than shallower slopes [*Pritchard et al.*, 2009; *Royden and Perron*, 2013]. If shocks develop, steep slopes can consume shallower slopes and part of the uplift history will be erased, resulting in spatiotemporal gaps. If $n=1$, the advective velocity is $v_\circ(PA)^m$ and uplift events map directly into changes of elevation. There is no convincing evidence for shock wave behavior which implies that $n=1$ [*Pritchard et al.*, 2009]. A more compelling argument is given by *Paul et al.* [2014] who examined residual misfits between observed and predicted river profiles as a function of n. They showed that global minima occur at, or near, $n=1$. These minima exist for different model regularizations and for different degrees of smoothing, suggesting that drainage inventories are poorly fitted when $n \neq 1$. Their results are consistent with some field studies, which imply that $n \sim 1$ [e.g., *Whittaker et al.*, 2007; *Whittaker and Boulton*, 2012].

Figure 1 shows the results of jointly inverting the Orange river and its longest tributaries that drain South Africa using the nonlinear inverse method of *Roberts et al.* [2012]. During each inversion run, $v_\circ$ and n were covaried to test the sensitivity of calculated uplift to changes in the value of erosional parameters [see *Paul et al.*, 2014]. The residual root-mean-squared (RMS) misfit, H, between observed and predicted river profiles is given by

$$H = \sqrt{\frac{1}{K}\sum_{i,j=1}^{I,J}\left(\frac{z_{ij}^{o} - z_{ij}^{c}}{\sigma}\right)^2}, \tag{3}$$

where z_{ij}^o and z_{ij}^c are observed and predicted river profile elevations, σ is the uncertainty associated with each elevation (typically ∼20 m away from narrow channels) [*Farr et al.*, 2007], I is the number of points along a given river profile, J is the number of river profiles, and K is total number of data points. Figure 1d shows that the RMS misfit has a global minimum at $n \sim 1$. At $n=1$, a reliable uplift rate history can be retrieved. If $n<1$, we found that the calculated peak uplift rate is higher and later. If $n>1$, the calculated peak uplift rate is both smaller and earlier, in agreement with the finding of *Goren et al.* [2014]. For example, if $n=0.7$, calculated peak uplift rate shifts forward to ∼9 Ma. If $n=1.5$, the calculated peak uplift rate shifts backward to ∼40 Ma. Figures 1f–1h shows how residual misfit varies as a function of erosional parameters for a set of forward models where $U(t)$ is fixed. Note that a global minimum occurs at $n=1$, although some trade-off between v, m, and n occurs. Combined with previously published results, these analyses suggest that it is reasonable to assume $n \sim 1$, which then justifies a linear inverse approach.

Rosenbloom and Anderson [1994] have suggested that κ is unlikely to be greater than 5×10^5 m^2 Ma^{-1}. Nevertheless, it is possible that κ varies by many orders of magnitude (e.g., 1–10^7 m^2 Ma^{-1}). In our inverse models, river profiles are sampled every 10–20 km, which implies that the minimum value of κ that can be resolved is 10^7 m^2 Ma^{-1} (i.e., $\kappa=l^2/T_l$, where $l=$ horizontal resolution and $T_l=$ longevity of a river). This value exceeds all reported estimates and implies that erosional diffusivity can be safely ignored. In other words, advective retreat of uplift signal is the dominant control and transport-limited processes are of negligible importance at the scales under consideration [e.g., *Berlin and Anderson*, 2007].

Finally, a parsimonious strategy assumes that both A, P, and the reference level (i.e., sea level) are invariant. In fact, A is undoubtedly modified by river capture events and precipitation rates vary with space and time. The integral solution of equation (11) suggests that significant temporal changes of A and P have a relatively minor effect on calculated uplift histories. Changes in A scale time, which is clear from the governing equation when diffusion is neglected. Since it is taken to a fractional power, A can vary by $\pm0.5A$ without adversely affecting calculated uplift rate histories. *Paul et al.* [2014] showed that their African results are essentially unchanged when precipitation rate is varied, provided P varies with a period of less than ∼10 Ma. They also showed that lithology and slope, curvature or steepness index correlate less well at wavelengths greater than several kilometers and that drainage planforms have probably been configured by Neogene dynamic support. *Czarnota et al.* [2014] showed that altering river profile lengths by 10–50 km has a small effect on calculated uplift rate histories. Finally, it can be shown that rapid glacioeustatic changes in sea level do not adversely affect the long-wavelength component of river profiles [e.g., *Miller et al.*, 2005].

A key outcome of earlier optimization schemes, which solve equation (1) in its general form, is that erosional parameter values must be constrained using independent observations of uplift and/or incision rate histories. Without careful calibration, uplift rate histories cannot be convincingly determined [e.g., *Royden and Perron*, 2013]. In some locations (e.g., southeast Australia, Colorado Plateau, and West Africa), local uplift and incision histories demonstrate how $v_\circ$, m, and n trade off against each other [*Stock and Montgomery*, 1999; *Czarnota et al.*, 2014]. Since our previous results are insensitive to published values of κ and since $n \sim 1$ gives the best fit to data, we can now formulate the linear inverse problem.

3. A Linear Inverse Model

3.1. Method of Characteristics

Our experience of solving the general optimization problem suggests that the evolving shape of a river profile can be approximated by

$$-\frac{\partial z}{\partial t} + vA^m\frac{\partial z}{\partial x} = U(x,t). \tag{4}$$

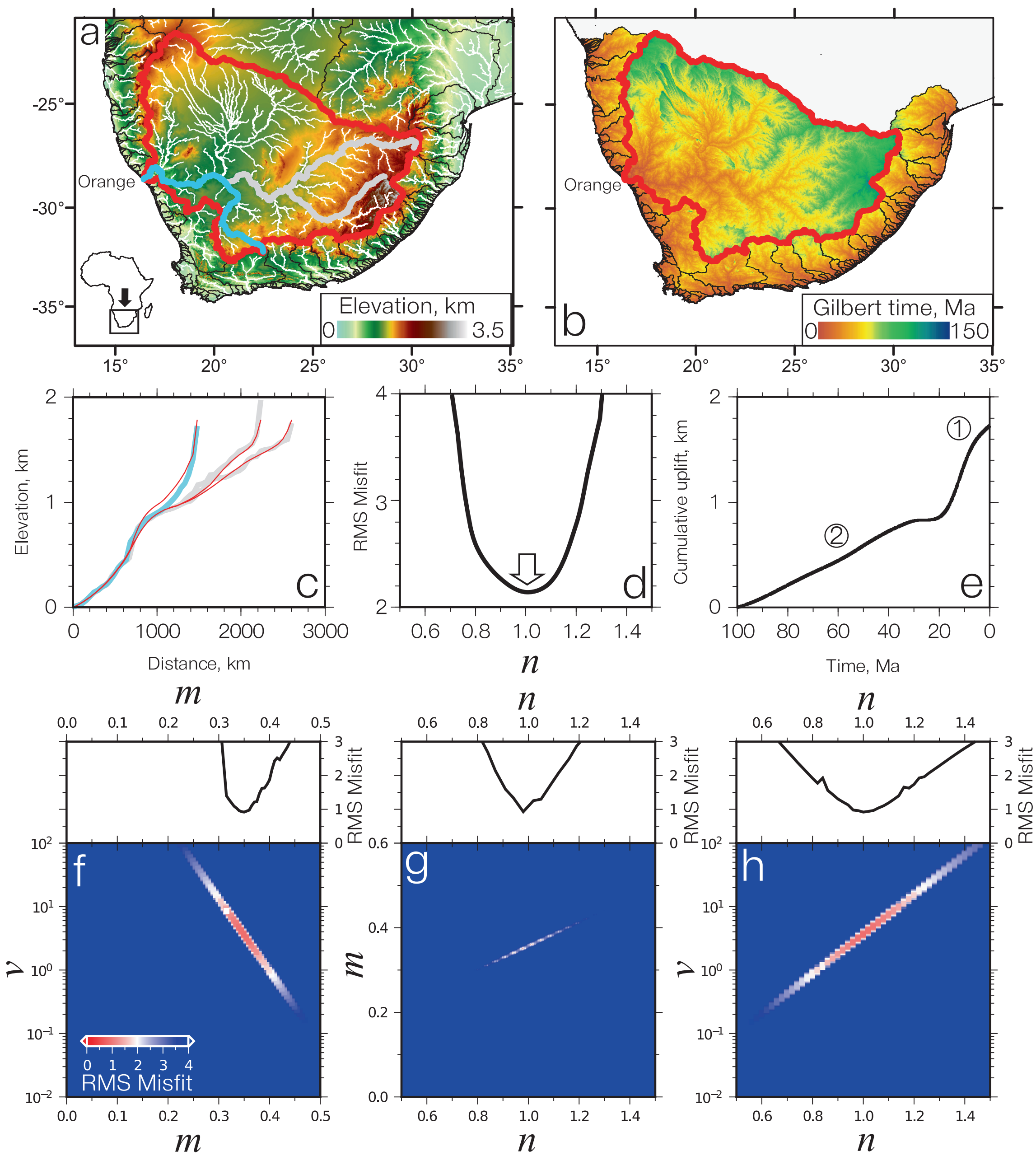

Figure 1. Inverse modeling of Orange river and its tributaries. (a) Topography and drainage of southern Africa. White lines = drainage network; black lines = drainage divides; red line = Orange catchment; gray/blue lines = modeled tributaries. (b) Landscape response time, τ_G, for map shown in Figure1a. (c) Joint inversion of three tributaries of Orange river for $U(t)$. Gray/blue lines = observed profiles; red lines = predicted profiles for $n = 1$. (d) Residual RMS misfit between observed and calculated river profiles as function of n from joint inversion. Arrow indicates global minimum at $n = 1$. (e) Cumulative uplift as function of time determined by general, nonlinear, optimization algorithm for single tributary of Orange river with $n = 1$ (blue lines in Figures 1a and 1c). Encircled numbers = principal uplift events (cf. linearized inversion; Figure 2c). (f) RMS misfit between observed and calculated Orange tributary (Figure 1c, blue line) when v and m are covaried in series of forward models with fixed uplift rate history. Input uplift history shown in Figure 1e. Misfit variation along trade-off relationship (red and white shading). (g) RMS misfit when m and n are covaried for fixed uplift rate history shown in Figure 1e. Misfit variation along trade-off relationship (red and white shading). (h) RMS misfit when v and n are covaried for fixed uplift rate history shown in Figure 1e. Misfit variation along trade-off relationship (red and white shading).

This kinematic wave equation can be solved using the well-known method of characteristics [e.g., *Lighthill and Whitham*, 1955; *Weissel and Seidl*, 1998]. The solution takes the form of $z(x,t) = z(x(t),t)$. Since

$$\frac{dz}{dt} = \frac{\partial z}{\partial t} + \frac{dx}{dt}\frac{\partial z}{\partial x} = \left(vA^m + \frac{dx}{dt}\right)\frac{\partial z}{\partial x} - U(x(t),t), \tag{5}$$

the solution can be written as a pair of ordinary differential equations

$$\frac{dx}{dt} = -vA^m, \tag{6}$$

$$\frac{dz}{dt} = -U(x(t),t). \tag{7}$$

Appropriate boundary conditions are

$$x = x^*,\ z = z^* \text{ at } t = 0 \tag{8}$$

$$\text{and } x = 0,\ z = 0 \text{ at } t = \tau_G. \tag{9}$$

The first boundary condition represents the present day, where at a position x^* along a river, the elevation is z^*. For position x^*, τ_G is termed the Gilbert Time. The second boundary condition represents a time in the past, τ_G, at which the characteristic curve intersects the river mouth (i.e., $x=0$) which occurs at sea level (i.e., $z=0$). From equations (6), (8), and (9), the Gilbert Time must satisfy

$$\tau_G = \int_0^{x^*} \frac{dx}{vA^m}. \tag{10}$$

A general solution for equations (6)–(9) can be written in integral form as

$$\tau_G - t = \int_0^{x(t)} \frac{dx}{vA^m} \text{ and} \tag{11}$$

$$z^* = \int_0^{\tau_G} U(x(t),t)\,dt. \tag{12}$$

This analysis closely follows the approaches used by *Lighthill and Whitham* [1955], *Luke* [1972], *Weissel and Seidl* [1998], *Smith et al.* [2000], and *Pritchard et al.* [2009].

3.2. Linear Least Squares Inversion

We wish to use a collection of observations, z^*, to invert the integral equation (12) for uplift rate, $U(x,t)$. First, the problem must be discretized in both space and time. Spatial discretization is accomplished by using a triangular mesh of the domain. Temporal discretization is accomplished by using a finite set of time intervals. In this way, uplift values can then be specified at a discrete set of spatial and temporal nodes as a vector of values given by $\mathbf{U}$. Values of uplift between these nodes are obtained by linear interpolation.

Given a discrete set of positions, x^*, and the upstream drainage area, A, along a river profile, equation (10) can be straightforwardly integrated using the trapezoidal rule. This integration yields values of Gilbert Time. Equation (11) is then used to obtain the characteristic curves. These curves are combined with linear interpolation to discretize equation (12), once again using the trapezoidal rule. The resultant matrix equation takes the form

$$\mathbf{z} = \mathrm{M}\mathbf{U} \tag{13}$$

for a set of elevations, $\mathbf{z}$, at different positions on different river profiles (Appendix A).

We can now invert equation (13) to find $\mathbf{U}$ from $\mathbf{z}$. To avoid the possibility of positive and negative oscillations, a nonnegativity constraint is normally imposed [*Parker*, 1994]. Since this particular problem is often underdetermined (i.e., M can have fewer rows than columns), it is also necessary to exploit a damped least squares approach. We minimize

$$|\mathrm{M}\mathbf{U} - \mathbf{z}|^2 + \lambda_S^2|\mathrm{S}\mathbf{U}|^2 + \lambda_T^2|\mathrm{T}\mathbf{U}|^2$$
$$\text{subject to } \mathbf{U} \geq 0, \tag{14}$$

which is a nonnegative least squares (NNLS) problem. Smoothing parameters are λ_S and λ_T , which control the regularization of this problem. The matrix S represents spatial smoothing and is given by

$$|\mathrm{S}\mathbf{U}|^2 = \int_S \int_{t=0}^{t_{\max}} |\nabla U|^2 \,\mathrm{d}t\,\mathrm{d}S. \tag{15}$$

Matrix T represents temporal smoothing and is given by

$$|\mathrm{T}\mathbf{U}|^2 = \int_S \int_{t=0}^{t_{\max}} \left|\frac{\partial U}{\partial t}\right|^2 \,\mathrm{d}t\,\mathrm{d}S. \tag{16}$$

Parameters λ_S and λ_T are chosen by analyzing the trade-off between smoothness and misfit [*Parker*, 1994]. We solve this NNLS problem using a limited memory version of the Broyden-Fletcher-Goldfarb-Shanno algorithm, L-BFGS-B, which is suited to problems with large sparse matrices [e.g., *Broyden et al.*, 1973]. We successfully benchmarked our results by implementing the slower active set algorithm of *Lawson and Hanson* [1974], which always converges optimally since it fulfills the Karush-Kuhn-Tucker conditions [e.g., *Kuhn and Tucker*, 1951]. In practice, computational cost is reduced by a factor of $\sim 10^4$ compared to nonlinear optimization methods [e.g., *Roberts et al.*, 2012].

Goren et al. [2014] and *Fox et al.* [2014] describe an alternative linear least squares algorithm that exploits an empirical Bayesian approach. In their algorithm, a prior model of the uplift history is first selected. This prior model uses a guess of the average uplift rate based upon channel elevation and upstream drainage area observations (see paragraph following equation (21) on page 6 of *Goren et al.* [2014]). Then, by updating this prior model with the observations, a posterior model is calculated. This posterior model stays close to the prior model and thus inherits some of its attributes. *Goren et al.* [2014] do not explicitly damp temporal gradients of uplift rate. Instead, they damp departures from their prior model by setting the value of Γ, the damping parameter. If $\Gamma \to \infty$, the posterior model converges toward the prior model (see their equation (21)). *Goren et al.* [2014] damp the spatial gradients of uplift rate by imposing a functional form on the spatial variation of uplift rate. In contrast, *Fox et al.* [2014] deliberately choose not to damp temporal gradients of uplift rate. They damp spatial gradients of uplift rate by specifying a correlation length scale parameter for their prior model. *Goren et al.* [2014] and *Fox et al.* [2014] show best fit solutions which have residual misfits of up to $\pm$150 m and $\pm$500 m, respectively.

4. Examples

4.1. Uplift as Function of Time

The linear inversion model can be used to fit a single river profile by allowing uplift rate to vary as a function of time alone. In southern Africa, there is excellent geologic and geophysical evidence for Neogene uplift of a series of three domes with diameters of $\sim$1000 km [*Giresse et al.*, 1984; *Burke*, 1996; *Partridge*, 1998; *Jackson et al.*, 2005; *Burke and Gunnell*, 2008; *Al-Hajri and White*, 2009]. A history of rapid uplift is constrained by emergent Plio-Pleistocene marine terraces, which suggest that in places modern uplift rates along the coastline exceed 0.3 mm/a [*Giresse et al.*, 1984; *Partridge and Maud*, 1987; *Partridge*, 1998; *Guiraud et al.*, 2010]. Offshore, erosional truncation of deltaic foreset deposits records 0.5–1 km of post-Pliocene (i.e., 5.3–0 Ma) uplift as well as an older Oligo-Miocene (25–30 Ma) uplift event [*Al-Hajri and White*, 2009]. Uplift histories can be used to calibrate the values of v and m [*Roberts and White*, 2010].

The South African dome is drained to the west by the Orange catchment, to the east by the Limpopo catchment, and to the south by a set of short, steep rivers [*Partridge*, 1998]. Figure 1b apparently shows differences in Gilbert time across drainage divides in South Africa, which have been interpreted as evidence that drainage divides migrate [*Willett et al.*, 2014]. It is difficult to resolve behavior at the head of a river since it represents a singularity and so juxtaposed Gilbert time discrepancies may be artifacts. *Roberts and White* [2010] showed that these southward draining rivers have prominent knickzones and so are highly disequilibrated. Previous inverse modeling suggests that several phases of Neogene uplift have occurred. In Figure 2, the Orange river has been inverted using erosional parameter values of $v = 3.62$ and $m = 0.35$ [*Paul et al.*, 2014]. These values were constrained using Miocene to present-day uplift rates [*Partridge*, 1998; *Partridge and Maud*, 2000; *Burke and Gunnell*, 2008]. Note that if A is rewritten as $A/A_\circ$, where $A_\circ$ is the maximum upstream area, v has the dimensions of velocity.

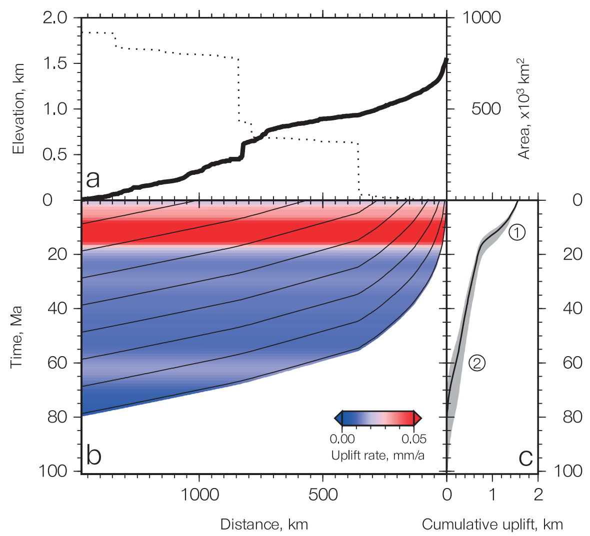

Figure 2. Linear inverse model of Orange river. (a) Solid line = observed river profile (i.e., blue line in Figure 1a); dotted line = observed upstream drainage area, *A*. (b) Solid lines = characteristic paths of river profile plotted for $vA^m = 3.62A^{0.35}$; colored bands = uplift rate history determined by linearized inverse model. (c) Solid line = cumulative uplift history obtained by integrating over uplift rate history; gray band = range of uncertainty for $A \pm 0.5A$; encircled numbers = principal uplift events (cf. Figure 1e).

Bearing in mind that uplift is permitted to vary as a function of time alone, our results suggest that peak uplift rates occurred between 20 Ma and the present day at rates which exceed 0.05 mm/a. The tail of cumulative uplift between 80 and 20 Ma is a consequence of assuming that uplift rate does not spatially vary. The results of linearized inversion are compatible with those obtained by *Pritchard et al.* [2009], *Roberts and White* [2010], and *Paul et al.* [2014].

4.2. Uplift as Function of Time and Space

Regional uplift varies as a function of time and space, which means that modeling individual river profiles by varying uplift rate as a function of time alone is of limited practical use. Furthermore, a single profile on its own cannot be used to determine the spatial variation of uplift rate. However, *Roberts et al.* [2012] showed that large inventories of river profiles could be jointly inverted by varying uplift through time and space. The linear inverse model can be used in a similar way. Here we show how continent-wide inventories of river profiles can be used, subject to appropriate calibration, to determine the spatial and temporal pattern of uplift of large regions. We chose to analyze Africa and Australia, which have previously been modeled using a general optimization approach [*Paul et al.*, 2014; *Czarnota et al.*, 2014].

4.2.1. Africa

The African continent is surrounded by passive margins [*Burke*, 1996]. Its physiography is strongly bimodal: subequatorial Africa is characterized by a broad $\sim 10^4 \times 10^4$ km superswell; northern Africa is generally low lying. Superimposed on this bimodal framework are smaller $\sim 1000 \times 1000$ km domal swells [e.g., *Holmes*, 1944, Figure 3]. The oldest oceanic lithosphere that abuts the African continent has residual depths of a few hundred meters [*Winterbourne et al.*, 2014]. These depth anomalies suggest that the domal swells intersecting the margins of Africa are dynamically supported by hundreds of meters (Figure 3a). Onshore, admittance studies of the relationship between gravity and topography suggest that the “egg-box” physiography of Africa is a response to the pattern of convective circulation beneath the plate [e.g., *Jones et al.*, 2012]. Simulations of mantle convection suggest that dynamic topography grew rapidly during the last 30 Ma [e.g., *Gurnis et al.*, 2000; *Moucha and Forte*, 2011]. However, these simulations fail to predict the present-day basin and swell morphology of African topography. Three lines of evidence indicate that prior to ~ 35 Ma, the African continent was low lying. First, the distribution of post-Albian marine deposits shows that large portions of North and East Africa were below sea level [e.g., *Sahagian*, 1988, Figure 3c]. Second, Paleogene laterites and lateritic gravels indicate that topographic gradients were low [*Burke and Gunnell*, 2008]. Finally, carbonate reef deposits fringed several African deltas in Paleogene times, which is consistent with negligible clastic efflux (Figure 3c). Since Oligocene times, sedimentary flux to Africa’s deltas has dramatically increased; there has been widespread basaltic magmatism, and peneplains have been warped [e.g., *Burke*, 1996; *Partridge*, 1998; *Walford et al.*, 2005, Figure 3d]. Here we jointly invert an inventory of river profiles to estimate the spatial and temporal patterns of topographic growth.

Seven hundred and four river profiles were extracted from a 3 arc sec (~ 90 × 90 m) SRTM digital elevation model using Esri flow routing algorithms. Rivers which drain domal swells (e.g., Bié, Namibia, and southern Africa) form radial patterns (Figure 3a). Their longitudinal profiles are strongly convex upward. Broad knickzones occur, which are tens of kilometers long and hundreds of meters high and traverse different

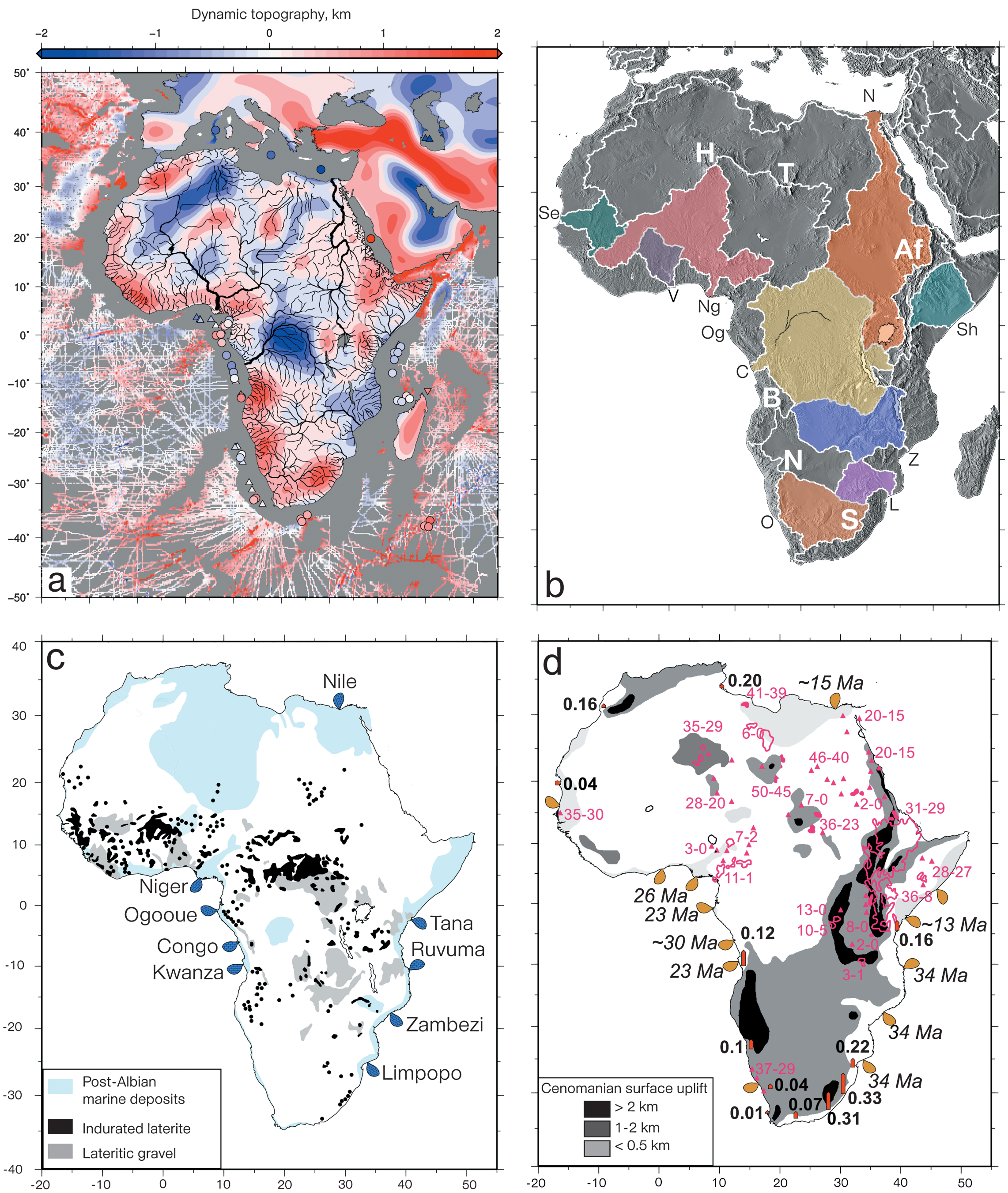

Figure 3. Independent geologic constraints for Africa. (a) Present-day dynamic support and drainage. Onshore red and blue pattern = positive and negative long-wavelength free-air gravity anomalies filtered to remove wavelengths < 800 km, with 10 mGal interval; offshore circles/triangles/filigree = residual bathymetric measurements [*Winterbourne et al.*, 2014]. Black drainage network = 704 rivers extracted from Shuttle Radar Topography Mission (SRTM) data set. (b) Major drainage basins. Se = Senegal, V = Volta, Ng = Niger, Og = Ogooue, C = Congo, O = Orange, L = Limpopo, Z = Zambezi, Sh = Shebelle, N = Nile. Domal swells: H = Hoggar, T = Tibesti, B = Bié, N = Namibia, S = South Africa, Af = Afar. (c) Pre-Oligocene paleogeography of Africa. Blue lobes = deltas with Paleogene reef deposits; light-blue shading = Cretaceous marine sedimentary rocks; gray/black circles = distribution of Cretaceous-Neogene laterites [*Sahagian*, 1988; *Burke*, 1996; *Burke and Gunnell*, 2008; *Paul et al.*, 2014]. (d) Neogene paleogeography; pink polygons = basaltic magmatism; yellow polygons = clastic deltaic deposition; numbered red arrows = observed Neogene-Recent uplift rates where height is proportional to rate in mm/a [*Burke*, 1996; *Paul et al.*, 2014].

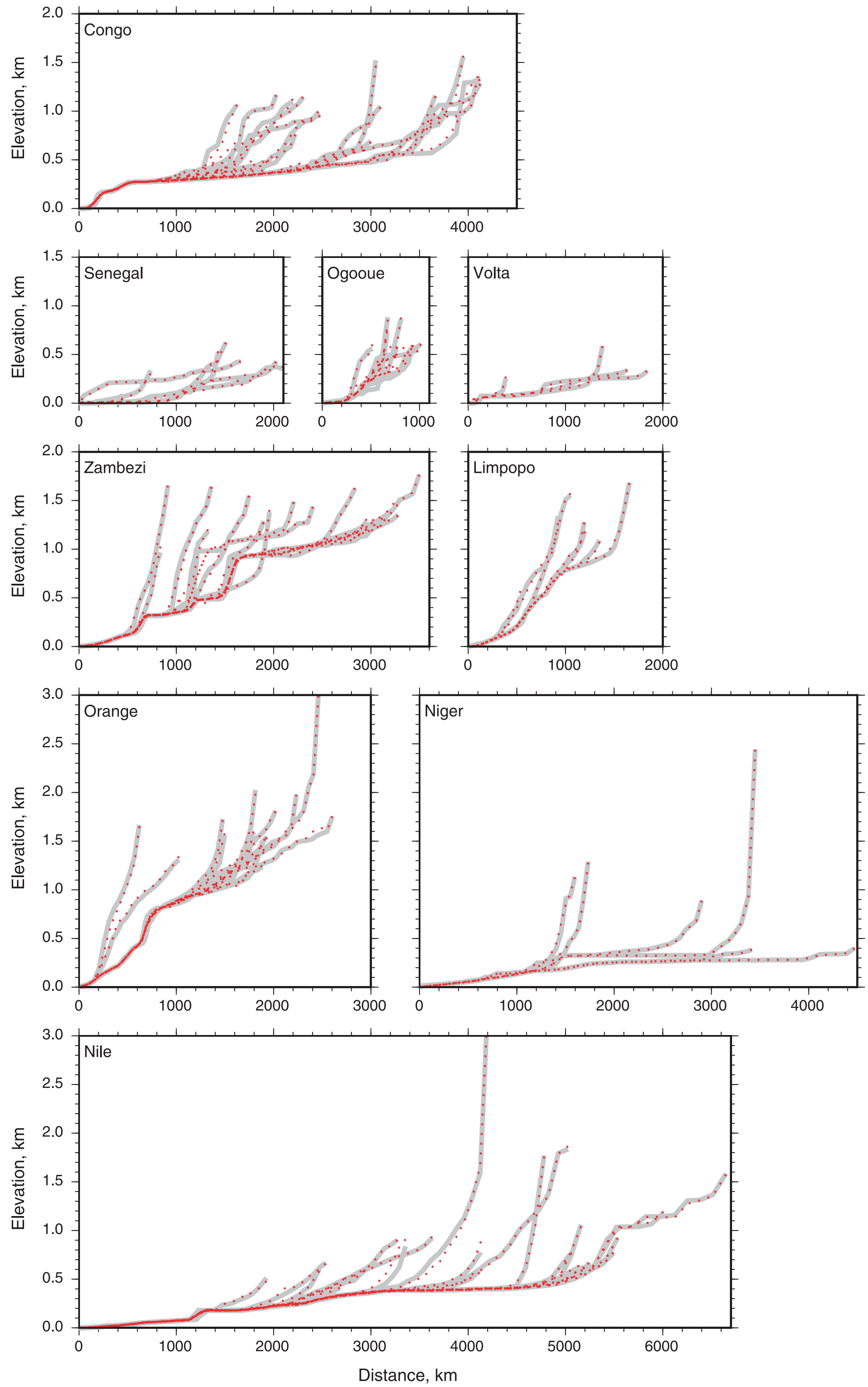

Figure 4. Inverse modeling of African river profiles arranged by catchment, which yields spatial and temporal patterns of cumulative uplift shown in Figure 5. Gray lines = observed river profiles; red-dotted lines = best fit theoretical river profiles generated using uplift history shown in Figure 5. Residual RMS misfit = 2.4.

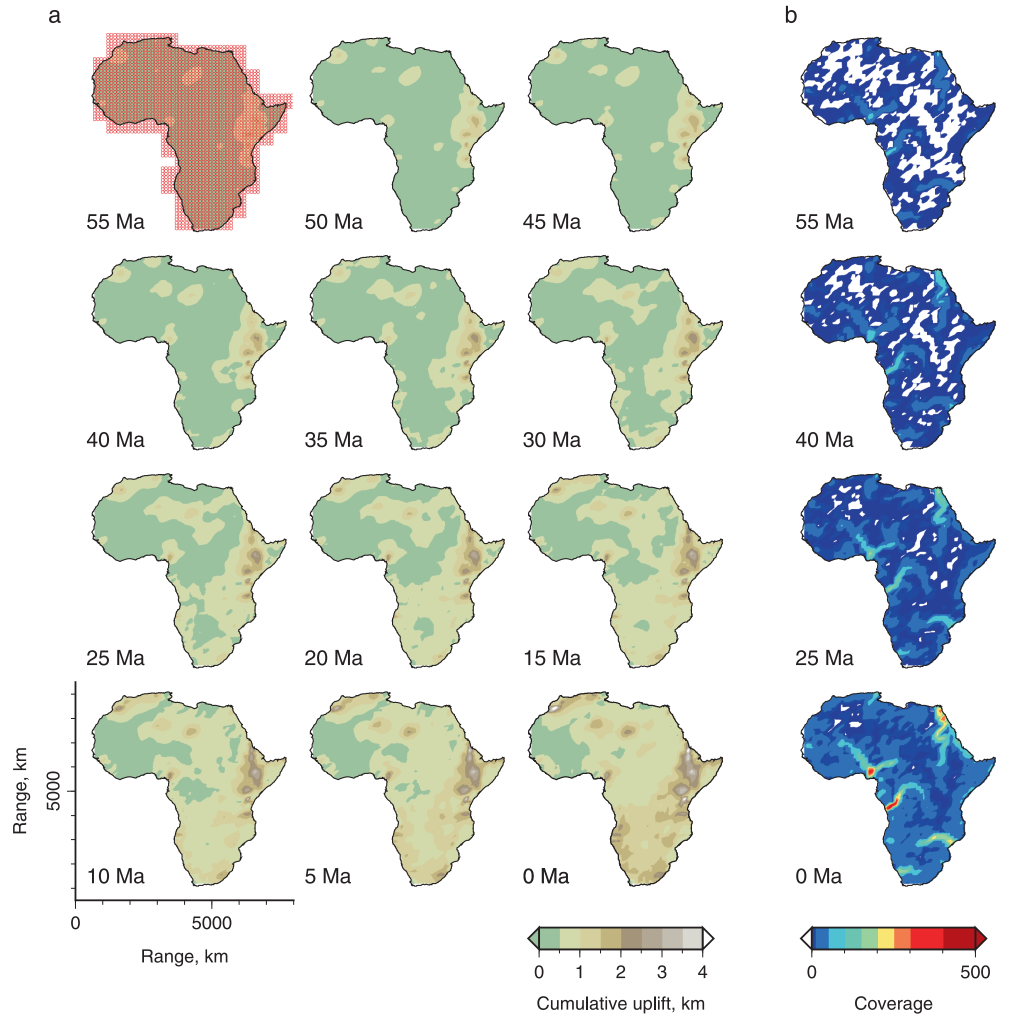

Figure 5. (a) Spatial and temporal pattern of cumulative uplift history for Africa from 55 Ma to present day at 5 Ma intervals. Red circles overlying left-hand panel = spatial regularization grid where triangular mesh = ⍁. (b) Selected panels at four different times, which show number of nonzero entries in model matrix, M, corresponding to a given uplift node.

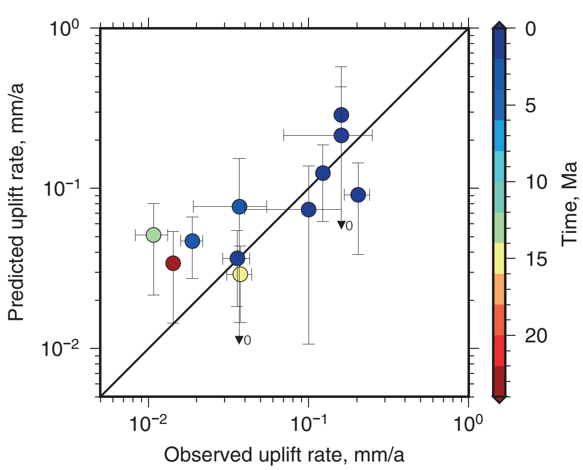

Figure 6. Comparison of observed and calculated uplift rates for Africa. Circles = weighted mean values of uplift rate where color indicates age (Table 1); vertical/horizontal lines with bars/arrows = uncertainties.

lithologies. In contrast, profiles of rivers draining North African swells (e.g., Hoggar, Tibesti, and Afar) are smoothly concave upward (Figure 4).

Most African river profiles can be accurately fitted (Figure 4). The largest discrepancies are mainly a result of coarse spatial and temporal gridding. Elsewhere, minor differences arise since our calculated rivers are smoother than observed ones. The predicted spatial and temporal patterns of cumulative uplift are shown in Figure 5a. These calibrated maps suggest that African topography grew rapidly over the last 30–40 Ma, in agreement with *Burke* [1996] and *Burke and Gunnell* [2008]. Domal uplift started in

Table 1. Observed and Calculated Uplift Rates for South Africa[a]

	Locality	Latitude	Longitude	Age (Ma)	Elevation (m)	Uplift Rate (mm/a)	Constraints
1	Pato's Kop	−33.34	27.37	44.85 ± 10.95	130	0.003 ± 0.001	*Partridge and Maud* [1987][b]
2	Birbury	−33.19	27.62	44.85 ± 10.95	200	0.005 ± 0.001	*Partridge and Maud* [1987][b]
3	Need's Camp	−33.09	27.73	44.85 ± 10.95	400	0.096 ± 0.002	*Partridge and Maud* [1987][b]
	Weighted mean					**0.014 ± 0.001**	
	Predicted rate					**0.034 ± 0.020**	
4	S.W. of Maputo	−27.35	31.17	15.5 ± 5.5	900	0.057 ± 0.018	*Partridge* [1998][b] and *Partridge and Maud* [2000][c]
5	Durban	−30.02	29.52	15.5 ± 5.5	1150	0.073 ± 0.023	*Partridge* [1998][b] and *Partridge and Maud* [2000][c]
6	East London	−32.05	28.28	15.5 ± 5.5	1100	0.070 ± 0.022	*Partridge* [1998][b] and *Partridge and Maud* [2000][c]
7	E. of George	−33.76	22.48	15.5 ± 5.5	400	0.025 ± 0.008	*Partridge* [1998][b] and *Partridge and Maud* [2000][c]
	Weighted mean					**0.037 ± 0.007**	
	Predicted rate					**0.029 ± 0.015**	
8	S.W. of Maputo			3.57 ± 1.76	600	0.222 ± 0.109	*Partridge* [1998][b] and *Partridge and Maud* [2000][c]
9	Durban			3.57 ± 1.76	900	0.334 ± 0.165	*Partridge* [1998][b] and *Partridge and Maud* [2000][c]
10	East London			3.57 ± 1.76	850	0.314 ± 0.156	*Partridge* [1998][b] and *Partridge and Maud* [2000][c]
11	E. of George			3.57 ± 1.76	200	0.074 ± 0.036	*Partridge* [1998][b] and *Partridge and Maud* [2000][c]
12	Greenwood Park	−29.79	31.02	4.26 ± 0.68	65	0.016 ± 0.003	*Erlanger et al.* [2012][d]
13	Bathurst	−33.74	26.46	4.47 ± 0.87	400	0.093 ± 0.018	*Partridge* [1998][b]
	Weighted mean					**0.019 ± 0.003**	
	Predicted rate					**0.047 ± 0.019**	
14	S. of P. Nolloth	−30.40	18.48	15.5 ± 5.5	250	0.016 ± 0.005	*Partridge* [1998][b] and *Partridge and Maud* [2000][c]
15	Saldanha bay	−32.99	17.96	13 ± 5	∼ 150	0.020 ± 0.010	*Roberts and Brink* [2002][e]
16	Hondeklip bay	−30.31	17.27	13 ± 5	∼ 90	0.008 ± 0.003	*Roberts and Brink* [2002][e]
	Weighted mean					**0.011 ± 0.002**	
	Predicted rate					**0.051 ± 0.029**	
17	S. of P. Nolloth	−30.40	18.48	3.57 ± 1.76	100	**0.037 ± 0.018**	*Partridge* [1998][b] and *Partridge and Maud* [2000][c]
	Predicted rate					**0.077 ± 0.077**	
18	Kuiseb R.	−23.34	15.74	1.6 ± 1.2	175 ± 75	**0.100 ± 0.060**	*Van der Wateren and Dunai* [2001][f]
	Predicted rate					**0.074 ± 0.063**	
19	AN40-2	−15.20	12.13	0.133 ± 0.010	15	0.114 ± 0.010	*Giresse et al.* [1984] and *Guiraud et al.* [2010][g]
20	AN57-1	−12.56	13.42	0.091 ± 0.006	11 ± 1	0.120 ± 0.020	*Giresse et al.* [1984] and *Guiraud et al.* [2010][g]
21	AN27	−12.56	13.42	0.071 ± 0.007	28 ± 3	0.390 ± 0.080	*Giresse et al.* [1984] and *Guiraud et al.* [2010][g]
22	AN47	−12.56	13.42	0.036 ± 0.003	9 ± 1	0.250 ± 0.050	*Giresse et al.* [1984] and *Guiraud et al.* [2010][g]
	Weighted mean					**0.123 ± 0.009**	
	Predicted rate					**0.124 ± 0.062**	
23	Tafoli	18.82	−15.05	0.099 ± 0.016	5 ± 1	0.054 ± 0.019	*Giresse et al.* [2000][h]
24	Tafoli	18.82	−15.05	0.258 ± 0.014	8 ± 2	0.032 ± 0.011	*Giresse et al.* [2000][h]
25	Tin Oueich	18.05	−15.83	0.122 ± 0.005	5 ± 1	0.041 ± 0.099	*Giresse et al.* [2000][h]
26	Tin Oueich	18.05	−15.83	0.241 ± 0.015	8 ± 2	0.034 ± 0.010	*Giresse et al.* [2000][h]
	Weighted mean					**0.036 ± 0.007**	
	Predicted rate					**0.036 ± 0.018**	

Table 1. (continued)

	Locality	Latitude	Longitude	Age (Ma)	Elevation (m)	Uplift Rate (mm/a)	Constraints
27	Agadir	30.52	−9.69	$0.115^{+0.075}_{-0.07}$	18 ± 0.5	**0.160 ± 0.010**	*Meghraoui et al.* [1998][h]
	Predicted rate					**0.287 ± 0.286**	
28	Somaâ	36.54	10.78	0.45 ± 0.113	96 ± 2	0.240 ± 0.110	*Elmejdoub and Jedoui* [2009][i]
29	Somaâ	36.54	10.78	0.27 ± 0.029	54 ± 4	0.200 ± 0.040	*Elmejdoub and Jedoui* [2009][i]
30	Somaâ	36.54	10.78	∼ 0.123	23 ± 17	0.190 ± 0.140	*Elmejdoub and Jedoui* [2009][i]
	Weighted mean					**0.204 ± 0.036**	
	Predicted rate					**0.091 ± 0.053**	
31	Similani	−4.29	39.58	$0.0265^{+0.0013}_{-0.0015}$	4 ± 2	**0.160 ± 0.090**	*Hori* [1970] and *Odada* [1996][j]
	Predicted rate					**0.214 ± 0.214**	

[a]Bold type indicates average observed and predicted rates.
[b]Biostratigraphic dating of marine terraces and correlation with warped peneplains.
[c]Biostratigraphic dating of river incision and $^{40}Ar/^{39}Ar$ dating of pedogenic rock.
[d]^{26}Al and ^{10}Be dating of marine terrace.
[e]Biostratigraphic dating of strandlines.
[f]^{21}Ne dating of fluvial incision rate between 2.8 and 0.4 Ma.
[g]$^{230}Th/^{234}U$, $^{231}Pa/^{231}U$ and ^{14}C dating of marine terraces.
[h]U-Th dating of marine terraces.
[i]Oxygen isotope stage (OIS) correlation of marine terraces, with U-series calibration from *Jedoui et al.* [2003].
[j]^{14}C dating of marine terraces.

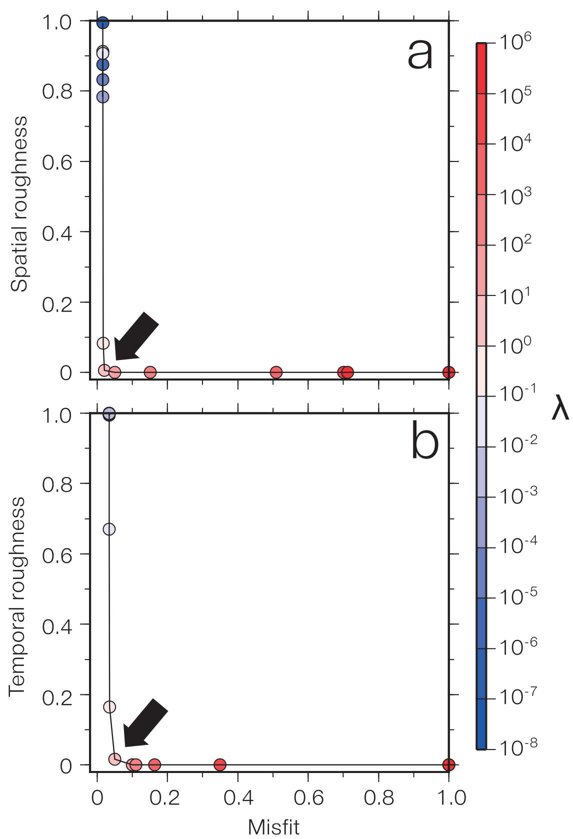

Figure 7. Model regularization. (a) Misfit, normalized by maximum misfit, as function of spatial smoothing for series of inverse models of 704 river profiles from Africa. Colored circles = individual inverse models for different values of λ_S; black arrow = optimal inverse model. (b) Normalized misfit as function of temporal smoothing. Colored circles = individual inverse models for different values of λ_T.

North and East Africa. For example, the Hoggar, Tibesti, and Afar swells appear early on, which is consistent with their magmatic histories [e.g., *Wilson and Guiraud*, 1992; *Permenter and Oppenheimer*, 2007]. After 30 Ma, the Afar Swell appears to extend southward along the East African Rift. Subequatorial topography grew more rapidly during the last 20 Ma, culminating in the appearance of the Bié, Namibian, and South African swells. This predicted diachronous growth of topography during Neogene times is largely coeval with the onset of mafic magmatism in North Africa and with increased sedimentary flux into coastal deltas [e.g., *Burke*, 1996; *Walford et al.*, 2005; *Guillocheau et al.*, 2012; *Paul et al.*, 2014]. Figure 6 compares our predicted rates with observed uplift rates based upon emergent marine terraces and uplifted surfaces (Table 1). The inverse algorithm is highly damped which means that rapid, short-wavelength, uplift rates along the West and southern Africa tend to be underestimated. Nonetheless, calculated rates are consistent with the long-term pattern of uplift determined from Pliocene marine terraces along the West African margin where a broad axis of uplift decays away from the Bié dome (Figure 5) [*Giresse et al.*, 1984; *Guiraud et al.*, 2010]. In southern Africa, stratigraphic evidence suggests that rapid Miocene and late Pliocene uplift events occurred at rates which are consistent with predicted values (Figure 6) [*Partridge and Maud*, 1987, 2000; *Roberts and*

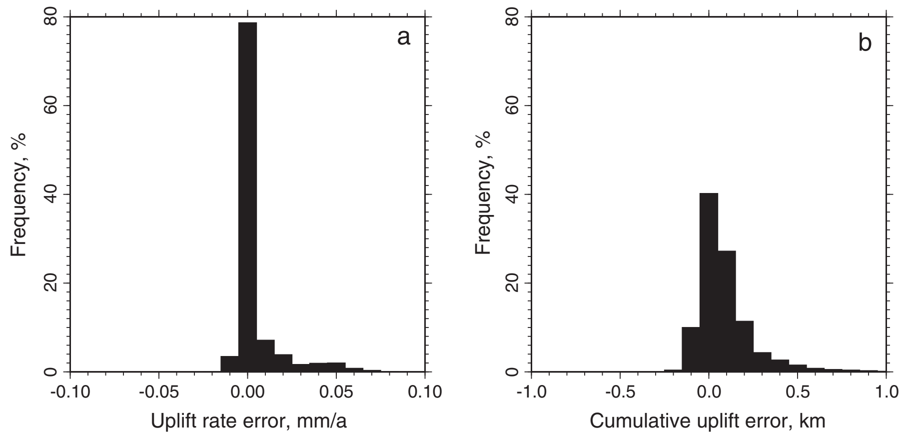

Figure 8. Systematic error analysis for Africa. (a) Difference between calculated uplift rates at all spatial and temporal nodes for original and modified (i.e., all elevations increased by 100 m) drainage inventories. (b) Difference between calculated cumulative uplift for original and modified drainage inventories.

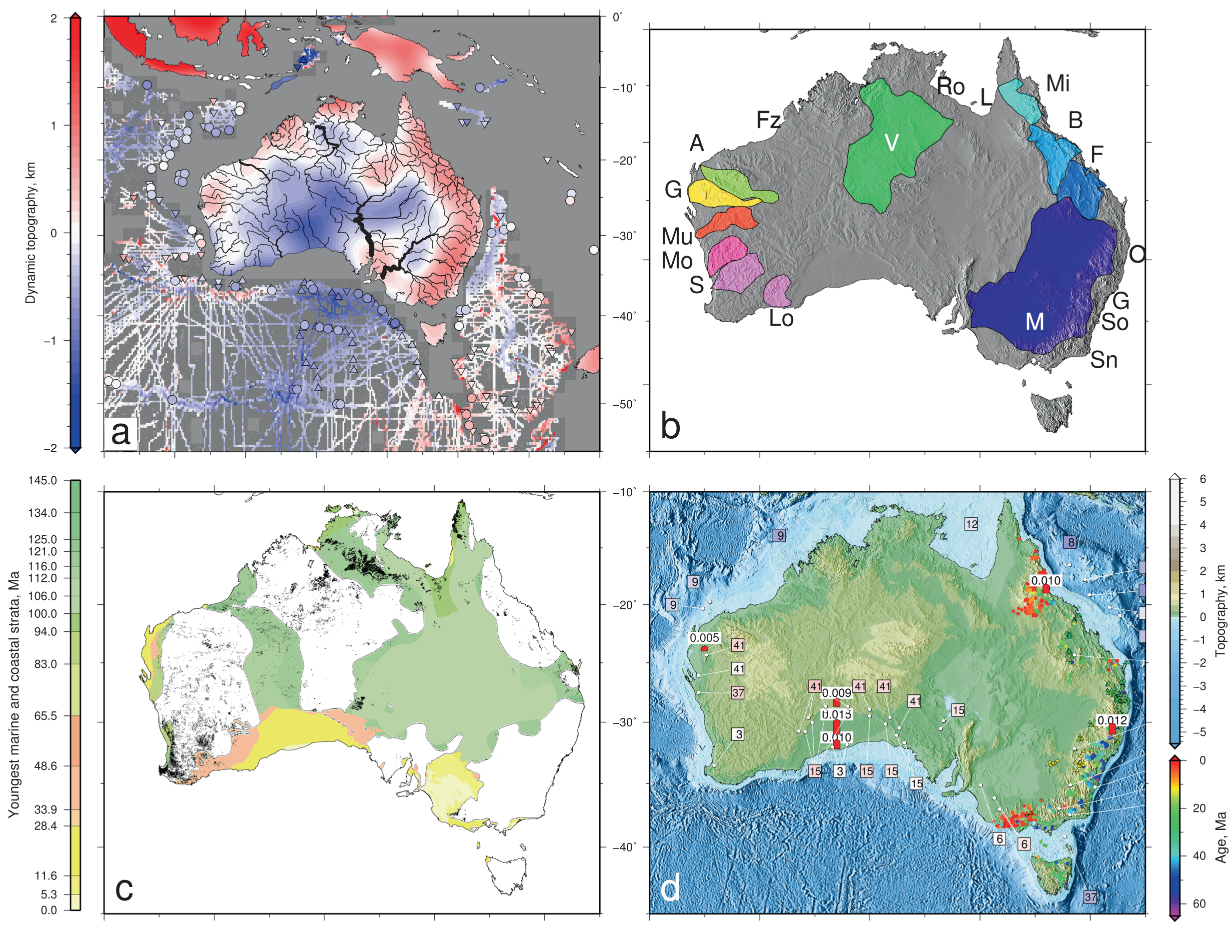

Figure 9. Independent geologic constraints for Australia. (a) Present-day dynamic support. Red and blue pattern onshore = positive and negative long-wavelength free-air gravity anomalies filtered to remove wavelengths < 800 km, at 10 mGal intervals; circles/triangles/filigree offshore = residual bathymetric measurements [*Winterbourne et al.*, 2014; *Czarnota et al.*, 2014]; black drainage network = 253 rivers extracted from SRTM data set. (b) Major drainage basins. V = Victoria, Fz = Fitzroy, A = Ashburton/Robe, G = Greenough, Mu = Murchison, Mo = Moore, S = Swan, Lo = Lort/Brandy Creek, M = Murray-Darling, Sn = Snowy, So = Shoalhaven, G = Grose, O = Oban, F = Fitzroy, B = Burdekin, Mi = Mitchell, L = Leichhardt, R = Roper. (c) Colored polygons = youngest marine and coastal strata [*Langford et al.*, 1995]. Black circles = distribution of Mesozoic and Cenozoic laterite deposits [*Raymond et al.*, 2012]. (d) Circles/triangles = mafic/bimodal magmatism; squares = regional uplift where color and number indicate magnitude and age in Ma [*Czarnota et al.*, 2014]. Numbered red arrows = uplift rates from emergent marine terraces where height is proportional to rate in mm/a [*Wellman*, 1987; *Langford et al.*, 1995; *Haig and Mory*, 2003; *Sandiford*, 2007].

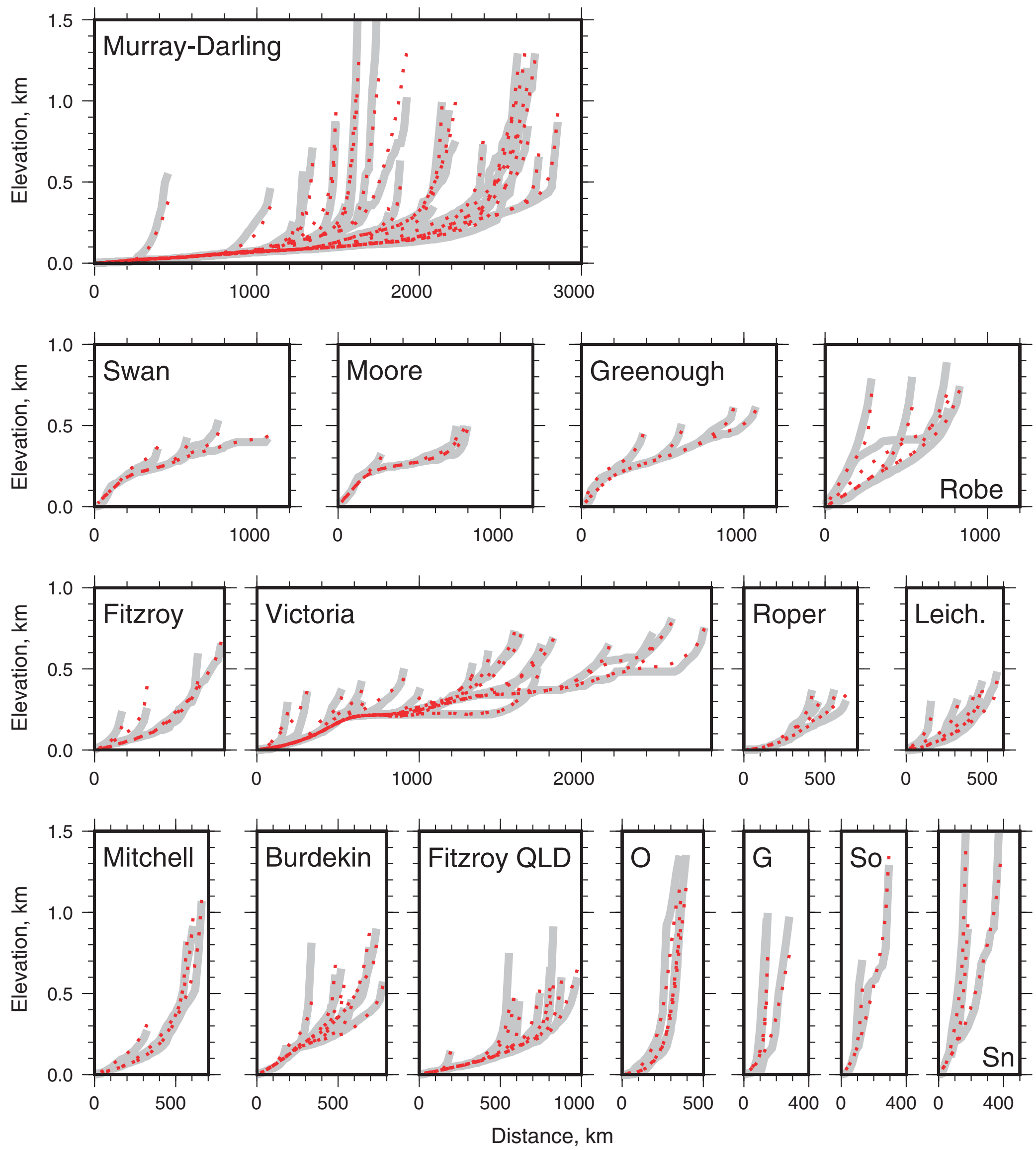

Figure 10. Inverse modeling of Australian river profiles arranged by catchment. Gray lines = observed river profiles; red-dotted lines = best fit theoretical river profiles generated using uplift history shown in Figure 11a; RMS misfit = 1.8. (bottom right) Four panels: O = Oban, G = Grose, So = Shoalhaven, and Sn = Snowy.

Brink, 2002]. In North and East Africa, calculated cumulative uplift rates are consistent with the emergence of Pleistocene-Recent marine terraces with elevations <100 m [*Hori*, 1970; *Elmejdoub and Jedoui*, 2009].

The spatial and temporal resolutions of cumulative uplift are determined by a combination of drainage density and river length. Longer rivers can record older uplift events, and in general, uplift events within the lower reaches of a drainage network are better resolved than those which occur further upstream. Figure 5b shows the number of drainage loci that constrain the uplift history of each cell within the mesh at different time intervals. Thus, African drainage networks appear capable of resolving the principal Cenozoic uplift events.

Finally, different degrees of spatial and temporal smoothing were systematically investigated by running suites of inverse models (Figures 7a and 7b). These models reveal an expected trade-off between model smoothness and misfit [*Parker*, 1994]. Acceptable models are smooth with small residual misfits. The effect of systematic error on calculated uplift was investigated by inverting a drainage inventory in which elevation along each river profile was everywhere increased by +100 m. Compared to the original inverse model

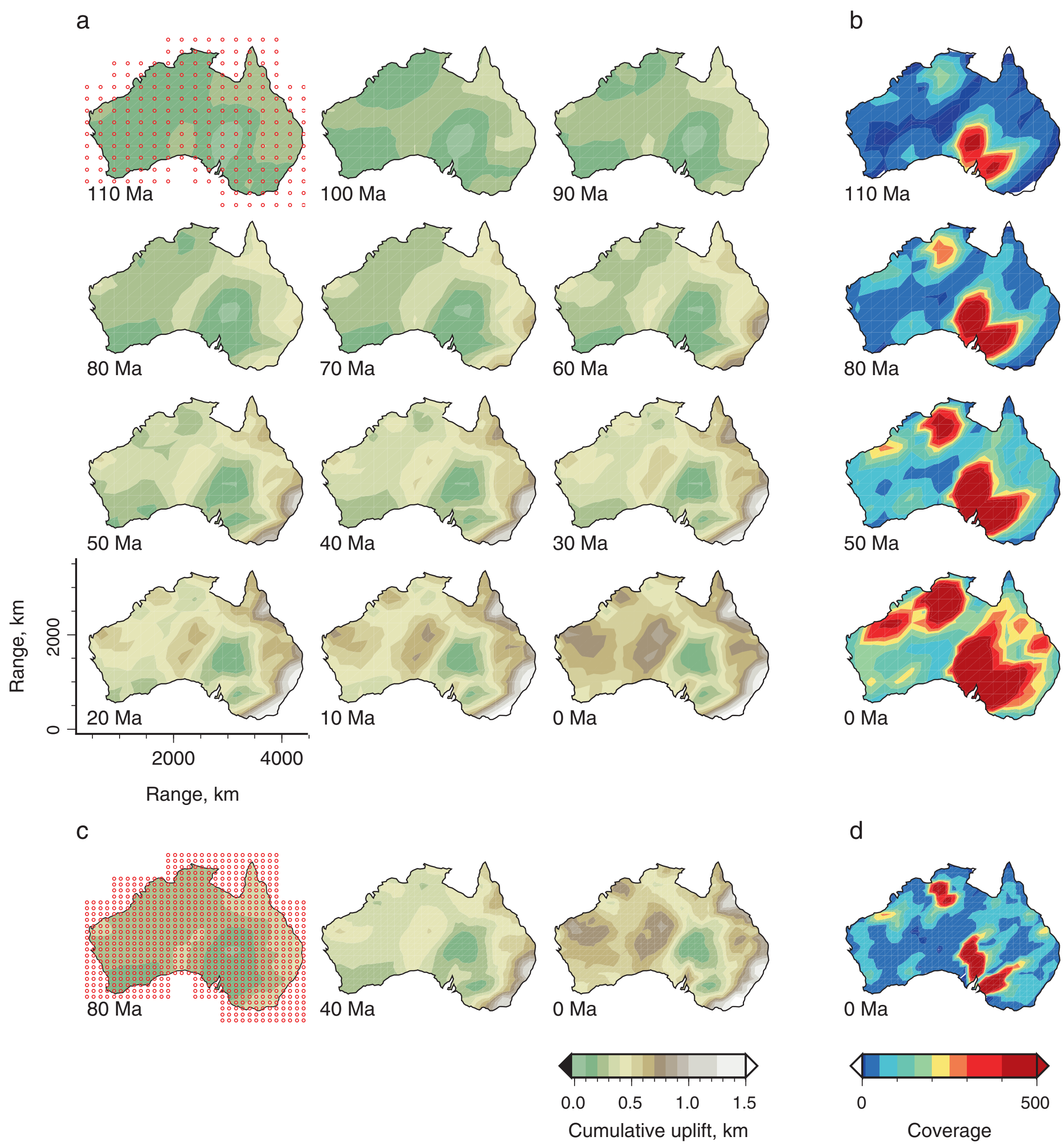

Figure 11. (a) Spatial and temporal pattern of cumulative uplift history for Australia from 110 Ma to present day at 10 Ma intervals. Red circles overlying left-hand panel = spatial regularization grid where triangular mesh = ◪. (b) Selected panels at four different times, which show number of nonzero entries in model matrix, M, corresponding to a given uplift node. (c and d) Inverse model with higher spatial resolution.

shown in Figure 5a, recovered uplift rates vary by less than ±0.01 mm/a and cumulative uplift by less than ±200 m at 89% of spatial and temporal nodes (Figure 8).

4.2.2. Australia

The physiography of Australia can be divided into four distinct regions: Eastern Highlands, Western Plateau, Central Lowlands, and Coastal Plains [e.g., *Quigley et al.*, 2010]. The Eastern Highlands, which reach elevations of 1–2 km, occupy the length of eastern Australia, which has been a passive margin since Jurassic times. At long wavelengths (>1000 km) free-air gravity data in eastern Australia are positive (+15–30 mGal; Figure 9a). Admittance studies of the spectral relationship between free-air gravity and topography suggest that the Eastern Highlands are dynamically supported by 0.5–1 km, which approximately coincides with the elevation of knickzones in eastern Australia (Shoalhaven and Snowy rivers of Figure 10) [*McKenzie and Fairhead*, 1997; *Czarnota et al.*, 2014]. Topography of the Western Plateau is more subdued than that of

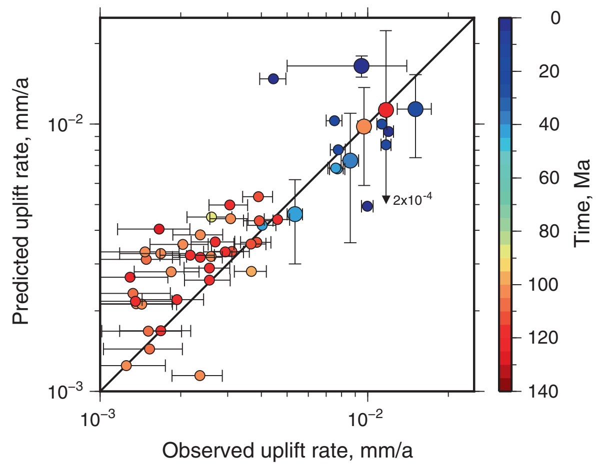

Figure 12. Comparison of observed and calculated uplift rates for Australia. Large circles = weighted mean values of uplift rate where color indicates age (Table 2) [*Wellman*, 1987; *Langford et al.*, 1995; *Haig and Mory*, 2003; *Sandiford*, 2007]. Small circles with error bars = rates calculated from gridded heights and ages of uplifted marine deposits with uncertainties of 5×10^{-4} mm/a [*Langford et al.*, 1995] (Figure 9c and Table 2); vertical/horizontal lines with bars/arrows = uncertainties.

the Eastern Highlands. However, substantial (tens of kilometers long, hundreds of meters high) knickzones occur close to the coastline, which suggests an actively eroding landscape (Figure 10: Swan, Moore, and Greenough). The Central Lowlands and Coastal Plains typically have elevations <100 m.

Offshore, the evolution of dynamic support is constrained by rapid Neogene subsidence of shallow water carbonate reef deposits (Figure 9d) [*Czarnota et al.*, 2014]. Onshore, uplift of southern Australia is recorded by Eocene (~50 Ma), Miocene (~15 Ma), and Pliocene (~5 Ma) marine terraces, which have elevations of ~0.5 km, 0.3 km, and 0.2 km, respectively [*Sandiford*, 2007]. The existence of Cretaceous coastal and marine strata indicate that most of Australia was at, or below, sea level until ~90 Ma. Uplift mainly occurred during the Cenozoic era (Figures 9c and 9d) [*Langford et al.*, 1995; *Haig and Mory*, 2003]. Cenozoic basaltic and intermediate magmatism peppers the eastern margin [see *Vasconcelos et al.*, 2009, and references therein]. Oligocene and younger igneous rocks in eastern Australia are deeply incised by rivers and record the growth of relief [*Young and McDougall*, 1993]. These data help to calibrate the erosional model. In southeastern Australia, 21 Ma old basalt flows have preserved the shapes of ancient river profiles [*Young and McDougall*, 1993].

Since river profiles at two different times are known, best fitting values of v and m can be identified [e.g., *Stock and Montgomery*, 1999; *Czarnota et al.*, 2014]. In southeastern Australia, $v = 5.96$ m$^{0.4}$/Ma and $m = 0.3$. We have used these values of v and m (Table 3) to invert an inventory of 253 Australian river

Table 2. Observed and Predicted Uplift Rates in Australia[a]

	Locality	Latitude	Longitude	Age (Ma)	Elevation (m)	Uplift Rate (mm/a)	Constraints
32	Nullabor	−28.70	127.00	~36	310 ± 23	**0.0086 ± 0.0006**	*Sandiford* [2007][b]
	Predicted rate					**0.0073 ± 0.0037**	
33	Nullabor	−31.00	127.00	~15	227 ± 34	**0.0151 ± 0.0022**	*Sandiford* [2007][b]
	Predicted rate					**0.0114 ± 0.0039**	
34	Nullabor	−32.20	127.00	~3	23 ± 8	**0.0095 ± 0.0045**	*Sandiford* [2007][b]
	Predicted rate					**0.0165 ± 0.0015**	
35	Pilbara	−24.00	115.00	39 ± 2	~190	**0.0054 ± 0.0045**	*Haig and Mory* [2003][c]
	Predicted rate					**0.0046 ± 0.0016**	
36	MacLeay R.	−31.00	152.00	120 ± 5	~1400	**0.0117 ± 0.0005**	*Wellman* [1987] and *Langford et al.* [1995][d]
	Predicted rate					**0.0113 ± 0.0111**	
37	Herbert R.	−19.00	146.00	103 ± 5	~1000	**0.0098 ± 0.0005**	*Wellman* [1987] and *Langford et al.* [1995][d]
	Predicted rate					**0.0091 ± 0.0039**	

[a]Bold type indicates average observed and predicted rates.
[b]Uplifted marine terraces.
[c]Marine sedimentary rocks.
[d]Youngest marine deposits.

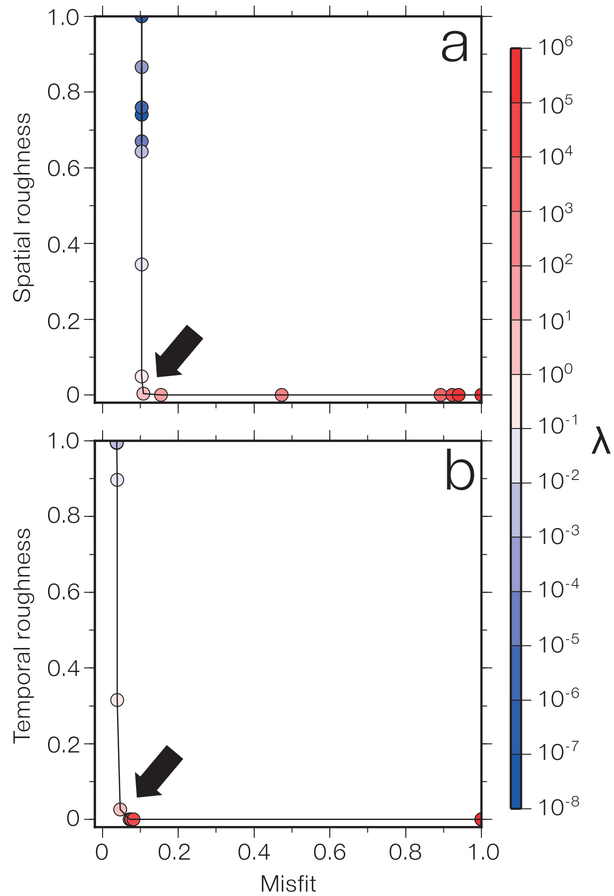

Figure 13. Model regularization. (a) Normalized misfit as function of spatial smoothing for series of inverse models of 253 river profiles from Australia (see Figure 7 for misfit calculation). Colored circles = individual inverse models for different values of λ_S; black arrow = optimal inverse model. (b) Normalized misfit as function of temporal smoothing. Colored circles = individual inverse models for different values of λ_T.

profiles as a function of the spatial and temporal uplift rate history. As before, river profiles were extracted from the 3 arc sec SRTM data set (Figures 9a and 9b) [*Czarnota et al.*, 2014]. These data were compared to satellite imagery, spot measurements of elevation, and published longitudinal profiles [e.g., *van der Beek and Bishop*, 2003; *Brown et al.*, 2011]. Apart from internally drained central regions, the fidelity of the extracted network is high.

Fits between observed and calculated river profiles are shown in Figure 10. The resultant spatial and temporal pattern of cumulative uplift is shown in Figure 11. Figures 11c and 11d show that shorter wavelength uplift can be resolved when a finer spatial grid is employed. However, using a finer resolution uplift grid increases the model's null space (Figure 11d). Our results suggest that the growth of Australian topography took place over the last 70–80 Ma. Eastern Australia has been uplifted by 1–1.5 km since ~70 Ma at maximum rates of 0.05–0.1 mm/a (Figure 11a). Western and central Australia have been uplift by 0.5–1 km since ~90 Ma. In Figure 12 we compare observed and predicted uplift rates. Predicted rates are consistent with ages of emergent marine terraces in southern Australia [e.g., *Sandiford*, 2007], and with the growth of relief recorded by river incision along the east coast [*Young and McDougall*, 1993] (Table 2). Our calculations are in broad agreement with those of *Czarnota et al.* [2014]. Figures 13a and 13b show the choice of smoothing parameter values used.

Table 3. Parameters Used for Inverse Modeling

Symbol	Description	Value	Units
z	Elevation		m
x	Distance along river		m
A	Upstream drainage area		m^2
t	Time		Ma
τ_G	Gilbert time		Ma
U	Uplift rate		mm a^{-1}
v	Advective coefficient of erosion	3.5–200	m^{1-2m} Ma^{-1}
v_o	Advective coefficient of erosion	0.5–25	m^{1-3m} Ma^{m-1}
m	Erosional constant	0.2–0.35	dimensionless
κ	Diffusivity	1–10^7	m^2 Ma^{-1}

5. Conclusions

By building upon the nonlinear optimization approach developed by *Pritchard et al.* [2009], *Roberts and White* [2010], and *Roberts et al.* [2012], we have described and applied a linear inverse model that can be used to fit substantial inventories of river profiles and determine spatial and temporal patterns of uplift rate (see also *Goren et al.* [2014] and *Fox et al.* [2014]). We show how this scheme is used to calculate uplift rate histories for single or multiple river profiles.

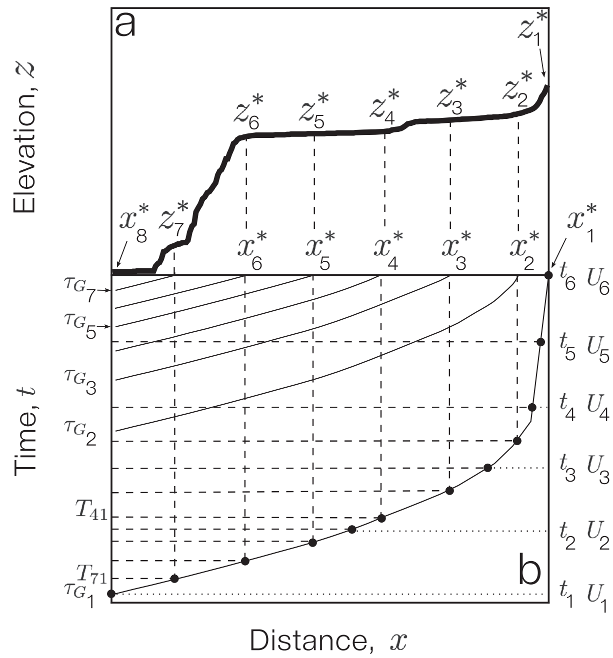

Figure A1. Diagram showing characteristic paths and notation for Ngunza River profile, Bié dome, West Africa.

The erosional model is a simplified version of the well-known stream power law that has a linear advective formulation. The governing equation is solved using the method of characteristics. Smooth uplift rate histories, which minimize the misfit between observed and theoretical river profiles are sought using a nonnegative least squares approach.

Our results suggest that Africa has largely been uplifted during the last 30 Ma. Its domal swells have a diachronous history of uplift, which is consistent with spot measurements of uplift estimated from subaerial exposed marine rocks and from truncated deltaic stratigraphy on the coastal shelf of West Africa (Figures 3c, 3d, and 5a). The Australian continent also underwent Cenozoic uplift. Eastern Australia was elevated by 1–1.5 km over the last 70 Ma. In southwest and southern Australia, our results are consistent with hundreds of meters of post 40 Ma uplift inferred from the elevation of Eocene and younger marine terraces (Figures 9c, 9d, and 10a).

In the examples shown, the erosional parameters, *v* and *m*, were calibrated using independently estimated incision or uplift rate histories. Parameters *v* and *m* trade off negatively with each other, and the values we use for Africa are approximately equivalent to $v = 200$ m$^{0.6}$ Ma^{-1} and $m = 0.2$ proposed by *Roberts et al.* [2012]. For Australia, *v* is a factor of 2 smaller. It is unclear why *v* and *m* vary from continent to continent.

Our results are encouraging since they suggest that drainage networks contain coherent patterns of knickzones that might not be caused by short-wavelength (<10 km) lithologic changes or by temporal discharge variations. Instead, it is conceivable that the evolution of these networks is controlled by spatial and temporal patterns of regional uplift. We propose that drainage networks might contain useful, albeit indirect, clues about topographic evolution and that a global analysis of drainage inventories might be a fruitful endeavor.

Appendix A: Discretization

Consider the example shown in Figure A1 where uplift rate is permitted to vary as a function of space and time. Three steps are used to determine an uplift rate history using the approach outlined in section 3. First, $dx/dt = -vA^m$ is integrated once. Second, the matrix, M, is constructed. Finally, inversion is carried out using a nonnegative linear least squares approach.

The time taken for a knickzone to travel along a characteristic path is given by equation (10) as

$$\tau_{G_j} = \int_{x_n^*}^{x_{n-1}^*} \frac{dx}{vA^m} + \int_{x_{n-1}^*}^{x_{n-2}^*} \ldots + \int_{x_{j+1}^*}^{x_j^*} \frac{dx}{vA^m}. \qquad \text{(A1)}$$

This equation is discretized using the trapezoidal rule where

$$\tau_{G_j} = \sum_{k=j}^{n} \frac{\left(x_k^* - x_{k+1}^*\right)}{2} \left(\frac{1}{vA\left(x_n^*\right)^m} + \frac{1}{vA\left(x_{n+1}^*\right)^m} \right), \qquad \text{(A2)}$$

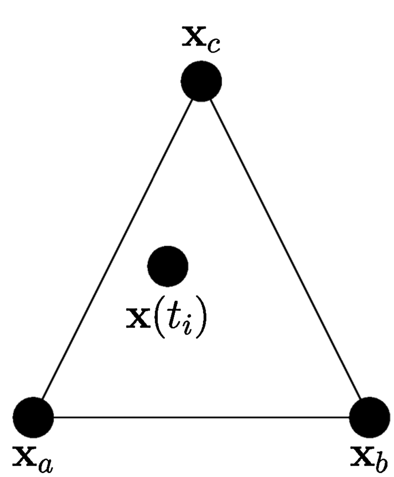

Figure A2. Barycentric coordinates $\mathbf{x}(t_i) = \alpha\mathbf{x}_a + \beta\mathbf{x}_b + \gamma\mathbf{x}_c$, where $\alpha + \beta + \gamma = 1$.

where $x_n^* = 0$ at the river mouth and $\tau_{G_n} = 0$ at the present day. In a similar way, equation (11) is approximated by

$$\tau_{G_j} - T_{ij} = \int_0^{x_i^*} \frac{dx}{vA^m} = \tau_{G_i} \quad \text{(A3)}$$

so that

$$T_{ij} = \tau_{G_j} - \tau_{G_i}, \quad i = j, j+1, \dots n. \quad \text{(A4)}$$

T_{ij} are values of time along the characteristic curve that is located at $x = 0$ and $t = \tau_{G_j}$ where distances and elevations along the river are known (i.e., $x(T_{ij})$=x_i). Uplift rate, U, is defined at discrete times (e.g., t_1, t_2, …, t_6) and at discrete positions. At intermediate times and positions, U is obtained by linear interpolation. Elevations are determined by integrating uplift rates along characteristic paths using the trapezoidal rule. Uplift rate histories are integrated between nodes whose loci are defined by t and x (e.g., black dots in Figure A1). Equation (12) is given by

$$z_j = \int_{S_{1_j}}^{S_{2_j}} U(\mathbf{x}(t), t)\, dt + \int_{S_{2_j}}^{S_{3_j}} \dots, \quad \text{(A5)}$$

where $\mathbf{x}(t)$ is the position in space along the characteristic curve at time t. This equation is approximated by

$$z_j^* = \sum_{k=1}^{m(j)} \frac{\left(S_{k+1,j} - S_{k_j}\right)}{2} \left[U\left(\mathbf{x}(S_{k+1,j}), S_{k+1,j}\right) + U(\mathbf{x}(S_{k,j}), S_{k,j})\right], \quad \text{(A6)}$$

where S_{ij} consists of dividing the integral up, both by times T_{ij}, at which the position of the river is known, and by times $t_1, t_2,$ …, at which uplift times are discretized. The number of points on characteristic curve j (i.e., 12 points on τ_{G_1}) is $m(j)$. At time T_{ij}, linear interpolation in time is carried out so that

$$U\left(T_{ij}, \mathbf{x}(T_{ij})\right) = U\left(T_{ij}, \mathbf{x}_i\right) = \frac{\left[T_{ij}^+ - T_{ij}\right] U\left(T_{ij}^+, \mathbf{x}_i\right) + \left[T_{ij} - T_{ij}^-\right] U\left(T_{ij}^-, \mathbf{x}_i\right)}{T_{ij}^+ - T_{ij}^-}, \quad \text{(A7)}$$

where T_{ij}^+ and T_{ij}^- are time nodes which bracket T_{ij}. At a time t_i, a linear interpolation in space is carried out so that

$$U(t_i, \mathbf{x}(t_i)) = \alpha U(t_i, \mathbf{x}_a) + \beta U(t_i, \mathbf{x}_b) + \gamma U(t_i, \mathbf{x}_c), \quad \text{(A8)}$$

where α, β, and γ are the barycentric weights for position $\mathbf{x}(t_i)$ (Figure A2). The mesh nodes of the triangle containing $\mathbf{x}(t_i)$ are $\mathbf{x}_a$, $\mathbf{x}_b$, and $\mathbf{x}_c$.

There is now a linear relationship between each river elevation, z_j^*, and uplift rate at each space and time node which can be cast in matrix form as

$$\mathbf{z} = M\mathbf{U}. \quad \text{(A9)}$$

Acknowledgments
G.G.R. was supported by BP Exploration and by an Imperial College junior research fellowship. We are grateful to A. Bump, R. Corfield, M. Falder, E. Jolley, L. Mackay, R. Parnell-Turner, and M. Thompson for their help and to A. Jackson for discussion. K. Czarnota and J. Paul generously shared their drainage inventories. Figures were generated using GMT 4.5.9. Software package for carrying out linear inverse modeling of river profiles is available from http://bullard.esc.cam.ac.uk/riverrun. It was written in Python using numpy, scipy, and FEniCS libraries [*Logg et al.*, 2012]. Digital elevation data used in this study can be downloaded from gdem.ersdac.jspacesystems.or.jp and srtm.csi.cgiar.org. University of Cambridge, Department of Earth Sciences contribution esc.3242.

References

Al-Hajri, Y., and N. White (2009), Scales of transient convective support beneath Africa, *Geol. Soc. Am. Bull.*, *37*(10), 883–886.
Anderson, R. S., and S. P. Anderson (2010), *Geomorphology: The Mechanics and Chemistry of Landscapes*, p. 651, Cambridge Univ. Press, Cambridge, U. K.
Brown, N. J., W. E. Featherstone, G. Hu, and G. M. Johnston (2011), AUSGeoid09: A more direct and more accurate model for converting ellipsoidal heights to AHD heights, *J. Spat. Sci.*, *56*(1), 27–37.
Broyden, C. G., J. E. Dennis Jr., and J. Moré (1973), On the local and superlinear convergence of quasi-Newton methods, *J. Inst. Math. Appl.*, *12*, 223–245.
Burke, K. (1996), The African plate, *S. Afr. J. Geol.*, *99*(4), 341–409.
Burke, K., and Y. Gunnell (2008), A continental-scale synthesis of geomorphology, tectonics, and environmental change over the past 180 million years, *Geol. Soc. Am. Mem.*, *201*, 1–66.
Berlin, M. M., and R. S. Anderson (2007), Modeling of knickpoint retreat on the Roan Plateau, western Colorado, *J. Geophys. Res.*, *112*, F03S06, doi:10.1029/2006JF000553.
Croissant, T., and J. Braun (2014), Constraining the stream power law: A novel approach combining a landscape evolution model and an inversion method, *Earth Surf. Dyn.*, *2*, 155–166.

Czarnota, K. C., G. G. Roberts, N. J. White, and S. Fishwick (2014), Spatial and temporal pattern of Australian dynamic topography from river profile modeling, *J. Geophys. Res. Solid Earth*, *119*, 1384–1424, doi:10.1002/2013JB010436.

Elmejdoub, N., and Y. Jedoui (2009), Pleistocene raised marine deposits of the Cap Bon peninsula (N–E Tunisia): Records of sea-level highstands, climatic changes and coastal uplift, *Geomorphology*, *112*, 179–189.

Erlanger, E. D., D. E. Granger, and R. J. Gibbon (2012), Rock uplift rates in South Africa from isochron burial dating of fluvial and marine terraces, *Geology*, *40*(11), 1019–1022.

Farr, T. G., et al. (2007), The Shuttle Radar Topographic Mission, *Rev. Geophys.*, *45*, RG2004, doi:10.1029/2005RG000183.

Flowers, R. M., B. P. Wernicke, and K. A. Farley (2008), Unroofing, incision, and uplift history of the southwestern Colorado Plateau from apatite (U-Th)/He thermochronometry, *Geol. Soc. Am. Bull.*, *120*(5/6), 571–587.

Fox, M., L. Goren, D. A. May, and S. D. Willett (2014), Inversion of fluvial channels for paleorock uplift rate in Taiwan, *J. Geophys. Res. Earth Surf.*, *119*, 1853–1875, doi:10.1002/2014JF003196.

Galloway, W. E., T. L. Whiteaker, and P. Ganey-Curry (2011), History of Cenozoic North American drainage basin evolution, sediment yield, and accumulation in the Gulf of Mexico basin, *Geosphere*, *7*(4), 938–973.

Ghosh, P., C. N. Garzione, and J. M. Eiler (2006), Rapid uplift of the altiplano revealed through ^{13}C–^{18}O bonds in paleosol carbonates, *Science*, *311*(5760), 511–515.

Giresse, P., C.-T. Hoang, and G. Kouyoumontzakis (1984), Analysis of vertical movements deduced from a geochronological study of marine Pleistocene deposits, southern coast of Angola, *J. Afr. Earth Sci.*, *2*(2), 177–187.

Giresse, P., J.-P. Barusseau, C. Causse, and B. Diouf (2000), Successions of sea-level changes during the Pleistocene in Mauritania and Senegal distinguished by sedimentary facies study and U/Th dating, *Mar. Geol.*, *170*, 123–139.

Goren, L., M. Fox, and S. D. Willett (2014), Tectonics from fluvial topography using formal linear inversion: Theory and applications to the Inyo Mountains, California, *J. Geophys. Res. Earth Surf.*, *119*, 1651–1681, doi:10.1002/2014JF003079.

Guiraud, M., A. Buta-Neto, and D. Quesne (2010), Segmentation and differential post-rift uplift at the Angola margin as recorded by the transform-rifted Benguela and oblique-to-orthogonal-rifted Kwanza basins, *Mar. Pet. Geol.*, *27*, 1040–1068.

Guillocheau, F., D. Rouby, C. Robin, C. Helm, N. Rolland, C. Le, C. de Veslud, and J. Braun (2012), Quantification and causes of the terrigeneous sediment budget at the scale of a continental margin: A new method applied to the Namibia–South Africa margin, *Basin Res.*, *24*, 3–30.

Gurnis, M., J. X. Mitrovica, J. Ritsema, and H.-J. van Heijst (2000), Constraining mantle density structure using geological evidence of surface uplift rates: The case of the African superplume, *Geochem. Geophys. Geosyst.*, *1*, 1020, doi:10.1029/1999GC000035.

Haig, D. W., and A. J. Mory (2003), New record of siliceous, marine, later Eocene from Kalbarri, Western Australia, *J. R. Soc. West. Aust.*, *86*, 107–113.

Holmes, A. (1944), *Principles of Physical Geology*, p. 532, Thomas Nelson, Edinburgh.

Hori, N. (1970), Raised coral reefs along the southeastern coast of Kenya, East Africa, *Rep. 5*, Dep. of Geog., Tokyo Univ., pp. 25–47, Tokyo.

Howard, A. D., and G. Kerby (1983), Channel changes in badlands, *Geol. Soc. Am. Bull.*, *94*, 739–752.

Jackson, M. P. A., M. R. Hudec, and K. A. Hegarty (2005), The great West African Tertiary coastal uplift: Fact or fiction? A perspective from the Angolan divergent margin, *Tectonics*, *24*, TC6014, doi:10.1029/2005TC001863.

Jedoui, Y., J. L. Reyss, N. Kallel, M. Montacer, H. Ben Ismail, and E. Davaud (2003), U-series evidence for two high Last Interglacial sea-levels in southeastern Tunisia, *Quat. Sci. Rev.*, *22*, 343–351.

Jones, S. M., B. Lovell, and A. G. Crosby (2012), Comparison of modern and geological observations of dynamic support from mantle convection, *J. Geol. Soc. London*, *169*, 745–758.

Kuhn, H. W., and A. W. Tucker (1951), Non-linear Programming, in *Proceedings of the Second Berkeley Symposium on Mathematical Statistics and Probability*, pp. 481–492, Univ. of Calif. Press, Berkeley.

Lague, D. (2014), The stream power river incision model: Evidence, theory and beyond, *Earth Surf. Processes Landforms*, *39*, 38–61.

Langford, R., G. Wilford, E. Truswell, and A. Isern (1995), *Palaeogeographic Atlas of Australia-Cainozoic, Cretaceous*, vol. 10, Aust. Geolog. Sur. Organ., Canberra, Aust.

Lawson, C. L., and R. J. Hanson (1974), *Solving Least Squares Problems*, Prentice-Hall, Englewood Cliffs, N. J.

Lighthill, M. J., and G. B. Whitham (1955), On kinematic waves, *Proc. R. Soc. London, Ser. A*, *229*(1178), 281–316.

Logg, A., K.-A. Mardal, and G. N. Wells (2012), *Automated Solution of Differential Equations by the Finite Element Method*, Springer, Berlin, doi:10.1007/978-3-642-23099-8.

Luke, J. C. (1972), Mathematical models for landform evolution, *J. Geophys. Res.*, *77*(14), 623–649.

McKenzie, D., and D. Fairhead (1997), Estimates of the effective elastic thickness of the continental lithosphere from bouguer and free-air gravity anomalies, *J. Geophys. Res.*, *102*(B12), 2460–2464.

Meghraoui, M., R. Outtani, A. Choukri, and D. Frizon De Lamotte (1998), Coastal tectonics across the South Atlas thrust front and the Agadir active zone, Morocco, in *Coastal Tectonics*, edited by I. S. Stewart and C. Vita-Finzi, *Geol. Soc. London Spec. Publ., 146*, pp. 239–253.

Miller, K., M. A. Kominz, J. V. Browning, J. D. Wright, G. S. Mountain, M. E. Katz, P. J. Sugarman, B. S. Cramer, N. Christie-Blick, and S. F. Pekar (2005), The Phanerozoic record of global sea-level change, *Science*, *310*, 1293–1298, doi:10.1126/science.1116412.

Mudd, S. M., M. Attal, D. T. Milodowski, S. W. D. Grieve, and D. A. Valters (2014), A statistical framework to quantify spatial variation in channel gradients using the integral method of channel profile analysis, *J. Geophys. Res. Earth Surf.*, *119*, 138–152, doi:10.1002/2013JF002981.

Moucha, R., and A. M. Forte (2011), Changes in African topography driven by mantle convection, *Nat. Geosci.*, *4*, 707–712, doi:10.1038/ngeo1235.

Odada, E. O. (1996), Geological evolution of coastal Kenya as inferred from sedimentary sequences and marine terraces, *Afr. Geosci. Rev.*, *3*(3), 1–18.

Parker, R. L. (1994), *Geophysical Inverse Theory*, Princeton Univ. Press, Princeton, N. J.

Partridge, T. C. (1998), Of diamonds, dinosaurs and diastophism; 150 million years of landscape evolution in southern Africa, *S. Afr. J. Geol.*, *101*(3), 167–184.

Partridge, T. C., and R. R. Maud (1987), Geomorphic evolution of southern Africa since the Mesozoic, *S. Afr. J. Geol.*, *90*(2), 179–208.

Partridge, T. C., and R. R. Maud (2000), Macro-scale geomorphic evolution of southern Africa, in *The Cenozoic of Southern Africa*, edited by T. C. Partridge and R. R. Maud, pp. 3–18, Oxford Univ. Press, New York.

Paul, J. D, G. G. Roberts, and N. J. White (2014), The African landscape through space and time, *Tectonics*, *32*, 898–935, doi:10.1002/2013TC003479.

Pedoja, K., et al. (2011), Relative sea-level fall since the last interglacial stage: Are coasts uplifting worldwide?, *Earth Sci. Rev.*, *108*, 1–15.

Permenter, J. L., and C. Oppenheimer (2007), Volcanoes of the Tibesti massif (Chad, northern Africa), *Bull. Volcanol.*, *69*, 609–626.

Pritchard, D., G. G. Roberts, N. J. White, and C. N. Richardson (2009), Uplift histories from river profiles, *Geophys. Res. Lett.*, *36*, L24301, doi:10.1029/2009GL040928.
Quigley, M. C., D. Clark, and M. Sandiford (2010), Tectonic geomorphology of Australia, *Geol. Soc. London. Spec. Publ.*, *346*, 243–265.
Raymond, O., S. Liu, R. Gallagher, L. M. Highet, and W. Zhang (2012), *Surface geology of Australia 1:2,500,000 scale, 2012 ed., [digital dataset], Geoscience Australia, Commonwealth of Australia, Canberra, Australia*.
Roberts, D. L., and J. S. Brink (2002), Dating and correlation of Neogene coastal deposits in the Western Cape (South Africa): Implications for Neotectonism, *S. Afr. J. Geol.*, *105*, 337–352.
Roberts, G. G., and N. J. White (2010), Estimating uplift rate histories from river profiles using African examples, *J. Geophys. Res.*, *115*, B02406, doi:10.0129/2009JB006692.
Roberts, G. G., J. D. Paul, N. White, and J. Winterbourne (2012), Temporal and spatial evolution of dynamic support from river profiles: A framework for Madagascar, *Geochem. Geophys. Geosyst.*, *13*, Q04004, doi:10.1029/2012GC004040.
Rosenbloom, N. A., and R. S. Anderson (1994), Hillslope and channel evolution in a marine landscape, Santa Cruz, California, *J. Geophys. Res.*, *99*(B7), 14,013–14,029.
Royden, L., and J. T. Perron (2013), Solutions of the stream power equation and application to the evolution of river longitudinal profiles, *J. Geophys. Res. Earth Surf.*, *118*, 497–518, doi:10.1002/jgrf.20031.
Sahagian, D. (1988), Epeirogenic motions of Africa as inferred from Cretaceous shoreline deposits, *Tectonics*, *7*(1), 125–138.
Sandiford, M. (2007), The tilting continent: A new constraint on the dynamic topographic field from Australia, *Earth Planet. Sci. Lett.*, *261*, 152–163.
Sklar, L. S., and W. E. Dietrich (1998), River longitudinal profiles and bedrock incision models: Stream power and the influence of sediment supply, in *Rivers Over Rock: Fluvial Processes in Bedrock Channels, Geophys. Monogr. Ser.,* vol. 107, edited by K. J. Tinkler and E. E. Wohl, pp. 237–260, AGU, Washington, D. C.
Sklar, L. S., and W. E. Dietrich (2001), Sediment and rock strength control on river incision into bedrock, *Geology*, *29*(12), 1087–1090.
Smith, T. R., G. E. Merchant, and B. Birnir (2000), Transient attractors: Towards a theory of the graded stream for alluvial and bedrock channels, *Comput. Geosci.*, *26*, 541–580.
Stock, J. D., and D. R. Montgomery (1999), Geologic constraints on bedrock river incision using the stream power law, *J. Geophys. Res.*, *104*(B3), 4983–4993.
Tanaka, K., R. Hataya, N. A. Spooner, D. G. Questiaux, Y. Saito, and T. Hashimoto (1997), Dating of marine terrace sediments by ESR, TL and OSL methods and their applicabilities, *Quat. Sci. Rev.*, *16*(3–5), 257–264.
Tomkin, J. H., M. T. Brandon, F. J. Pazzaglia, J. R. Barbour, and S. D. Willett (2003), Quantitative testing of bedrock incision models for the Clearwater River, NW Washington State, *J. Geophys. Res.*, *108*(B6), 2308, doi:10.1029/2001JB000862.
van der Beek, P., and P. Bishop (2003), Cenozoic river profile development in the Upper Lachlan catchment (SE Australia) as a test of quantitative fluvial incision models, *J. Geophys. Res.*, *108*(B6), 2309, doi:10.1029/2002JB002125.
Van der Wateren, F. M., and T. J. Dunai (2001), Late Neogene passive margin denudation history—Cosmogenic isotope measurements from the central Namib desert, *Global Planet. Change*, *30*, 271–307.
Vasconcelos, P. M., K. M. Knesel, B. E. Cohen, and J. A. Heim (2009), Geochronology of the Australian Cenozoic: A history of tectonic and igneous activity, weathering, erosion, and sedimentation, *Aust. J. Earth Sci.*, *55*, 865–914.
Wellman, P. (1987), Eastern Highlands of Australia; their uplift and erosion, *BMR J. Aust. Geol. Geophys.*, *4*, 373–382.
Walford, H. L., N. J. White, and J. C. Sydow (2005), Solid sediment load history of the Zambezi Delta, *Earth Planet. Sci. Lett.*, *238*, 49–63.
Weissel, J. K., and M. A. Seidl (1998), Inland propagation of erosional escarpments and river profile evolution across the southeastern Australian passive continental margin, in *Rivers Over Rock: Fluvial Processes in Bedrock Channels, Geophys. Monogr. Ser. 107*, edited by K. J. Tinkler and E. E. Wohl, pp. 189–206, AGU, Washington, D. C.
Whipple, K. X., and G. E. Tucker (1999), Dynamics of the stream-power river incision model: Implications for height limits of mountain ranges, landscape response timescales, and research needs, *J. Geophys. Res.*, *104*(B8), 17,661–17,674.
Whipple, K. X., and G. E. Tucker (2002), Implications of sediment-flux-dependent river incision models for landscape evolution, *J. Geophys. Res.*, *107*(B2), 2039, doi:10.1029/2000JB000044.
Wilson, M., and R. Guiraud (1992), Magmatism and rifting in Western and Central Africa, from late Jurassic to recent times, *Tectonophysics*, *213*, 203–225.
Willett, S. D., S. W. McCoy, T. J. Perron, L. Goren, and C.-Y. Chen (2014), Dynamic reorganization of river basins, *Science*, *343*, 1049–1168, doi:10.1126/science.1248765.
Winterbourne, J., N. White, and A. Crosby (2014), Accurate measurements of residual topography in the oceanic realm, *Tectonics*, *33*, 982–1015, doi:10.1002/2013TC003372.
Whittaker, A. C., and S. J. Boulton (2012), Tectonic and climatic controls on knickpoint retreat rates and landscape response times, *J. Geophys. Res.*, *117*, F02024, doi:10.1029/2011JF002157.
Whittaker, A. C., P. A. Cowie, M. Attal, G. E. Tucker, and G. P. Roberts (2007), Contrasting transient and steady-state rivers crossing active normal faults: New field observations from the Central Apennines, Italy, *Basin Res.*, *9*, 529–556.
Young, R., and I. McDougall (1993), Long-term landscape evolution: Early Miocene and modern rivers in southern New South Wales, Australia, *J. Geol.*, *101*, 35–49.